39. Pearson JM, Schultze AE, Jean PA, Roth RA. Platelet participation in liver injury from Gram-negative bacterial lipopolysaccharide in the rat. Shock. 1995;4:178–86.
40. Itoh H, Cicala C, Douglas GJ, Page CP. Platelet accumulation induced by bacterial endotoxin in rats. Thromb Res. 1996; 83:405–19.
41. Nakamura M, Shibazaki M, Nitta Y, Endo Y. Translocation of platelets into Disse spaces and their entry into hepatocytes in response to lipopolysaccharides, interleukin-1 and tumour necrosis factor: the role of Kupffer cells. J Hepatol. 1998;28: 991–9.
42. Pinzani M, Gesualdo L, Sabbah GM, Abboud HE. Effects of platelet-derived growth factor and other polypeptide mitogens on DNA synthesis and growth of cultured rat liver fat-storing cells. J Clin Invest. 1989;84:1786–93.
43. Dirks RP, Bloemers HP. Signals controlling the expression of PDGF. Mol Biol Rep. 1996;22:1–24.
44. Borkham-Kamphorst E, van Roeyen CRC, Ostendorf T, Floege J, Gressner AM, Weiskirchen R. Pro-fibrogenic potential of PDGF-D in liver fibrosis. J Hepatol. 2007;46:1064–74.
45. Czochra P, Klopcic B, Meyer E, Herkel J, Garcia-Lazaro JF, Thieringer F, et al. Liver fibrosis induced by hepatic overexpression of PDGF-B in transgenic mice. J Hepatol. 2006;45: 419–28.
46. Friedman SL. Mechanisms of hepatic fibrogenesis. Gastroenterology. 2008;134:1655–69.
47. Maass T, Thieringer FR, Mann A, Longerich T, Schirmacher P, Strand D, et al. Liver specific overexpression of platelet-derived growth factor-B accelerates liver cancer development in chemically induced liver carcinogenesis. Int J Cancer. 2011;128:1259–68.
48. Li X, Eriksson U. Novel PDGF family members: PDGF-C and PDGF-D. Cytokine Growth Factor Rev. 2003;14:91–8.
49. Kelly JD, Haldeman BA, Grant FJ, Murray MJ, Seifert RA, Bowen-Pope DF, et al. Platelet-derived growth factor (PDGF) stimulates PDGF receptor subunit dimerization and intersubunit trans-phosphorylation. J Biol Chem. 1991;266:8987–92.
50. Tanaka M, Nakashima O, Wada Y, Kage M, Kojiro M. Pathomorphological study of Kupffer cells in hepatocellular carcinoma and hyperplastic nodular lesions in the liver. Hepatology. 1996; 24:807–12.

Pegylated Interferon-α2a Inhibits Proliferation of Human Liver Cancer Cells *In Vitro* and *In Vivo*

Hironori Kusano[1*], Jun Akiba[1], Sachiko Ogasawara[1], Sakiko Sanada[1], Makiko Yasumoto[1], Masamichi Nakayama[1], Keiko Ueda[1], Kosuke Ueda[1], Takashi Kurita[1], Keita Todoroki[1], Yumi Umeno[1], Osamu Nakashima[2], Hirohisa Yano[1]

1 Department of Pathology, Kurume University School of Medicine, Kurume, Fukuoka, Japan, **2** Department of Clinical Laboratory Medicine, Kurume University Hospital, Kurume, Fukuoka, Japan

Abstract

Purpose: We investigated the effects of pegylated interferon-α2a (PEG-IFN-α2a) on the growth of human liver cancer cells.

Methods: The effect of PEG-IFN-α2a on the proliferation of 13 liver cancer cell lines was investigated *in vitro*. Cells were cultured with medium containing 0–4,194 ng/mL of PEG-IFN-α2a, and after 1, 2, 3, or 4 days of culture, morphologic observation and growth assay were performed. After hepatocellular carcinoma (HCC) cells (HAK-1B and KIM-1) were transplanted into nude mice, various doses of PEG-IFN-α2a were subcutaneously administered to the mice once a week for 2 weeks, and tumor volume, weight, and histology were examined.

Results: PEG-IFN-α2a inhibited the growth of 8 and 11 cell lines in a time- and dose-dependent manner, respectively, although the 50% growth inhibitory concentrations of 7 measurable cell lines on Day 4 were relatively high and ranged from 253 ng/mL to 4,431 ng/mL. Various levels of apoptosis induction were confirmed in 8 cell lines. PEG-IFN-α2a induced a dose-dependent decrease in tumor volume and weight, and a significant increase of apoptotic cells in the tumor. Subcutaneous administration of clinical dose for chronic hepatitis C (3 μg/kg, 0.06 μg/mouse) was effective and induced about 30-50% reduction in the tumor volume and weight as compared with the control.

Conclusions: Although *in vitro* anti-proliferative effects of PEG-IFN-α2a were relatively weak, PEG-IFN-α2a induced strong anti-tumor effects on HCC cells *in vivo*. The data suggest potential clinical application of PEG-IFN-α2a for the prevention and treatment of HCC.

Citation: Kusano H, Akiba J, Ogasawara S, Sanada S, Yasumoto M, et al. (2013) Pegylated Interferon-α2a Inhibits Proliferation of Human Liver Cancer Cells *In Vitro* and *In Vivo*. PLoS ONE 8(12): e83195. doi:10.1371/journal.pone.0083195

Editor: Diego Calvisi, Institut für Pathologie, Greifswald, Germany, Germany

Received August 19, 2013; **Accepted** November 10, 2013; **Published** December 12, 2013

Funding: This study was supported in part by the Sarah Cousins Memorial Fund, Boston, Massachusetts, and by a Grant-in-Aid from the Ministry of Health, Labor and Welfare of Japan. The funders had no role in study design, data collection and analysis, decision to publish, or preparation of the manuscript.

Competing interests: The authors have declared that no competing interests exist.

* E-mail: kusano_hironori@kurume-u.ac.jp

Introduction

Interferons (IFNs) are types of cytokine that are produced by host cells, such as leukocytes, in response to inflammation. Since IFNs possess antiviral activity, antiproliferative activity and various immunoregulatory activities, IFN therapy is used to treat patients with chronic viral hepatitis or certain types of cancer including malignant melanoma, acquired immunodeficiency syndrome-related Kaposi's sarcoma and some hematopoietic malignancies [1,2]. Lai et al also showed that recombinant IFNα is useful in prolonging survival among patients with inoperable hepatocellular carcinoma (HCC) [3]. In addition, some studies showed IFN therapy might prevent either occurrence or recurrence after initial curative therapy of HCC, such as liver resection and radiofrequency ablation, in patient with chronic viral hepatitis [4–7]. This cancer preventive effect of IFNs is regarded mainly as results of their antiviral effect and the consequent suppression of inflammation, and might be due to their direct antitumor effect against clinically undetectable HCC as well. The detailed mechanism of the antitumor effect of IFNs, however, remains obscure.

Pegylated interferon-α2a (PEG-IFN-α2a) and pegylated interferon-α2b (PEG-IFN-α2b), which are used to treat patients with chronic hepatitis C virus (HCV) or B virus (HBV) infection, are modified IFNs that have longer serum half-life in body than non-pegylated forms of IFNs, therefore they can be given to

patients only once a week, whereas a standard IFN without pegylation used to be injected up to three to five times a week. This once-a-week injection of pegylated IFNs in combination with daily oral dosing of the nucleoside analogue ribavirin has substantially improved the rate of sustained virological response in patients with chronic HCV infection and got a position as the first line therapy [8,9]. We previously reported that PEG-IFN-α2b which contains 12 kDa polyethylene glycol (PEG) has stronger antitumor effects *in vivo* than non-pegylated IFNs and this result might be indicating that continuous IFNs exposure to cancer cells in body is more effective than continual injection [10]. On the basis of above-described background, we examined the growth inhibitory effects of PEG-IFN-α2a which contains two chains of 20 kDa PEG and has the longest serum half-life among clinically available IFNs on liver cancer cell lines *in vitro* and *in vivo*.

Methods

Cell Lines and Cell Culture

This study used 11 HCC cell lines (KIM-1, KYN-1, KYN-2, KYN-3, HAK-1A, HAK-1B, HAK-2, HAK-3, HAK-4, HAK-5, and HAK-6) and 2 human combined hepatocellular and cholangiocarcinoma (CHC) cell lines (KMCH-1 and KMCH-2). These HCC and CHC cell lines were originally established in our laboratory, and each cell line retains the morphological and functional features of the original tumor as described elsewhere [11–20]. Since tumorigenicity is higher in HAK-1B and KIM-1 cells than in the other 11 cell lines that we have, we used these two cell lines for *in vivo* study.

The cells were grown in Dulbecco's Modified Eagle Medium (Nissui Seiyaku, Co., Japan) supplemented with 2.5% heat-inactivated (56°C, 30 min) fetal bovine serum (FBS, Bioserum, Victoria, Australia), 100 U/mL penicillin, 100 μg/mL streptomycin (GIBCO BRL/Life Technologies, Inc., Gaithersburg, MD) and 12 mmol/L sodium bicarbonate, in a humidified atmosphere of 5% CO_2 in air at 37°C.

IFN and Reagents

PEG-IFN-α2a (PEGASYS®, Chugai Pharmaceutical Co., Ltd., Tokyo, Japan) with the specific activity of 1.4 X 10^7 IU/mg protein and non-pegylated IFN-α2a (Miltenyi Biotec GmbH, Bergisch Gladbach, Germany) with that of 2.0 X 10^8 IU/mg protein were used in the study.

Anti-bromodeoxyuridine (BrdU) antibody and fluorescein isothiocyanate-conjugated goat anti-mouse immunoglobulin (FITC-GAM) were purchased from Becton Dickinson Immunocytometry Systems USA (San Jose, CA); control normal mouse IgG_1, from DAKO (Glostrup, Denmark); rat antibody against mouse endothelial cells (anti-CD34, clone MEC14.7), from Serotec Co., UK; and mouse monoclonal antibody against human α-smooth muscle actin (SMA) that cross-reacts with mouse α-SMA (clone 1A4).

Effects of PEG-IFN-α2a on the Proliferation of HCC and CHC Cell Lines *in vitro*

The effects of PEG-IFN-α2a on the growth of the cultured cells were examined with colorimetry using 3-(4,5-dimethylthiazol-2yl)-2,5-diphenyl tetrazolium bromide (MTT) assay kits (Chemicon, Temecula, CA) as described elsewhere [18,21]. Briefly, the cells (1.5~8 X 10^3 cells per well) were seeded on 96-well plates (Nunc, Inc, Roskilde, Denmark), cultured for 24 hours, and the culture medium was changed to a new medium with or without PEG-IFN-α2a (0.016, 0.064, 0.256, 1.024, 4.096, 16.4, 65.5, 262, 1,048, or 4,194 ng/mL). After culturing for 24, 48, 72 or 96 hours, the number of viable cells was measured with ImmunoMini NJ-2300 (Nalge Nunc International, Tokyo, Japan) by setting the test wavelength at 570 nm and the reference wavelength at 630 nm. To keep the optical density within linear range, all experiments were performed while the cells were in the logarithmic growth phase.

Quantitative analysis of apoptotic cells induced by PEG-IFN-α2a

HAK-1B or KIM-1 cells cultured with medium alone (control), non-pegylated IFN-α2a (10 ng/ml=2,000 IU/ml) or PEG-IFN-α2a (144 ng/ml=2,000 IU/ml) for 72 hours were stained with the Annexin V-EGFP (enhanced green fluorescent protein) Apoptosis Detection Kits (Medical & Biological Laboratories Co., Ltd.) according to the manufacturer's instructions. After staining, the cells were analyzed using a FACScan (Becton Dickinson Immunocytometry Systems, San Jose, CA), and Annexin V-EGFP-positive apoptotic cell rate was determined.

Morphological Observation

For morphological observation under a light microscope, cultured cells were seeded on Lab-Tek tissue culture chamber slides (Nunc, Inc.), cultured with or without PEG-IFN-α2a (262, 1,048 or 4,194 ng/mL) for 72 hours, fixed for 10 min in Carnoy's solution, and stained with hematoxylin-eosine (HE).

Effects of PEG-IFN-α2a on HCC Cell Proliferation in Nude Mice

All animal experiments were approved by the institutional committee for animal experiments in Kurume University School of Medicine (Permit Number: 1334), and conducted according to the Guide for the Care and Use of Laboratory Animals of the National Institute of Health and the Regulations for Animal Experimentation of Kurume University School of Medicine. Mice were killed by cervical dislocation under diethyl ether anesthesia, and all efforts were made to minimize suffering. Cultured HAK-1B or KIM-1 (10^7 cells/mouse) was subcutaneously (s.c.) injected into the backs of 5-week-old female BALB/c athymic nude mice (Clea Japan, Inc., Osaka, Japan). Five to seven days later when the largest diameter of the tumor, which was measured by using caliper, reached approximately 5~10 mm (Day 0), tumor volume (mm^3) was calculated in the equation 'the largest diameter X (the smallest diameter)^2 X 0.5', and then the mice were divided into 5 groups (n=8 each). Tumor volume was measured on Day 0, 1, 2, 4, 6, 8, 10, 12, and 14. Mouse body weight was measured on Day 0,

8, and 14. After 2-week treatment, mice were killed on Day 15 and the actual tumor weight was also measured. In experiment 1, the 5 groups of 8 mice received either phosphate-buffered saline (PBS) (Control) or PBS with the different dosages of PEG-IFN-α2a (0.06–60 μg) once a week for 2 consecutive weeks (Day 1 and Day 8). The clinical dose of PEG-IFN-α2a in chronic hepatitis C treatment is about 3 μg/kg and is equivalent to the lowest dose (0.06 μg/mouse=840 IU/mouse) in this experiment. After killing, resected tumors were used for morphological studies (e.g., HE staining and immunohistochemistry) and Enzyme-linked immunosorbent assay (ELISA) analysis. Every mouse received an intraperitoneal injection of 1 mg of BrdU 30 min before killing. In experiment 2, to examine the difference between non-pegylated and pegylated IFNs, 5 groups of 8 mice received either PBS (Control), PBS with 0.0042 or 0.042 μg of IFN-α2a (840 or 8,400 IU, respectively), or PBS with 0.06 or 0.6 μg of PEG-IFN-α2a (840 or 8,400 IU, respectively). In this experiment, tumor weights on Day 15 and numbers of apoptotic cells were compared among the groups.

Morphological Examination of the Subcutaneous Tumors of Nude Mice

The number of cells showing the characteristics of apoptosis (e.g., cytoplasmic shrinkage, chromatin condensation, and nuclear fragmentation) was counted in at least three 0.25 mm^2-areas within an HE-stained specimen, and the average number per area was obtained. The TUNEL technique (ApopTag® Peroxidase *In Situ* apoptosis Detection Kits, CHEMICON International, Inc, CA) was used to detect apoptotic cells, and the average number of TUNEL-positive cells per area was obtained, as described above. The specimens were also immunostained for incorporated BrdU using BrdU Staining Kits (Oncogene Research Products, Boston, MA), and the average number of positive cells per area was obtained as described above. In addition, double-immunostaining was performed with anti-mouse endothelial cell antibody, anti-human α-SMA antibody, Histofine simple stain mouse MAX-PO (Rat) kits (Nichirei, Tokyo, Japan), and HistoMouse™-plus kits to detect artery-like blood vessels as described in our previous report [21,22]. The number of double-immunostaining-positive blood vessels in the tumor was counted on each specimen. Granulation tissue within the tumor were excluded in counting of blood vessels. The size of the counted area was measured by tracing the outline displayed on a computer monitor using Mac SCOPE (MITANI Corp., Chiba, Japan). From the obtained number of vessels per unit area (mm^2), the group mean was obtained for group comparison.

Enzyme-linked immunosorbent assay (ELISA)

Portions of the resected xenograft tumors were homogenized in 500 μl of ice-cold Ca^{2+} and Mg^{2+}-free PBS containing 100 mg/ml phenymethylsulfonyl fluoride using a pellet pestle. The mixture was centrifuged for 10 min (12,000 g, 4°C), and the supernatant was stored at -20°C until use. After the determination of the amount of the tissue protein in the supernatant using a BCA protein assay reagent (Pierce, Rockford, IL), the amount of basic fibroblast growth factor (bFGF) and IL-8 was measured by using commercially available ELISA kits (R&D Systems, Minneapolis, MN).

Statistics

Comparisons of estimated tumor volume and colorimetric cell growth were performed using two-factor factorial ANOVA and Student's *t*-test, respectively. The other data comparisons were performed using the Mann-Whitney U test.

Results

Effects of PEG-IFN-α2a on Liver Cancer Cell Proliferation *in vitro*

Twenty-four hours after the addition of 4,194 ng/mL of PEG-IFN-α2a, mild increase in the relative viable cell number occurred in 9 cell lines (all cell lines except KYN-2, HAK-1A, HAK-6, and KMCH-1). However, after 72 hours or later, a 10% or more decrease in the cell number occurred in all cell lines (Figure 1A). In HAK-2, HAK-3, and HAK-4, HAK-6, and KMCH-2, proliferation was suppressed up to 72 hours and the cell number reached a plateau or slightly increased thereafter. In the other 8 cell lines, proliferation was suppressed to varying degrees up to 96 hours.

The relative viable cell number was suppressed in 11 cell lines (all cell lines except HAK-1A and KMCH-2) in a dose-dependent manner after the 96 hours-incubation with PEG-IFN-α2a (Figure 1B). In 7 cell lines (HAK-1B, KMCH-1, KIM-1, KYN-1, HAK-6, KYN-3, and KYN-2), the number was suppressed to 50% or less with 4,194 ng/mL of PEG-IFN-α2a, and the 50% inhibitory concentration (IC50) was 253 ng/mL for HAK-1B, 670 ng/mL for KMCH-1, 1,105 ng/mL for KIM-1, 1,128 ng/mL for KYN-1, 1,302 ng/mL for HAK-6, 1,524 ng/mL for KYN-3, and 4,431 ng/mL for KYN-2. No relationship was detected between the histological differentiation level of the original tumor and sensitivity to the anti-proliferative effect of PEG-IFN-α2a.

Seventy-two hours after adding 4,194 ng/mL of PEG-IFN-α2a, 8 cell lines (all cell lines except KYN-3, HAK-1A, HAK-2, HAK-3, and KMCH-2) showed characteristics of apoptosis, e.g., cytoplasmic shrinkage, chromatin condensation, and nuclear fragmentation, in various degrees and in a dose-dependent manner (Figure 2). The appearance of apoptosis was further confirmed in HAK-1B and KIM-1 cells cultured with 10 ng/ml (=2,000 IU/ml) of IFN-α2a or 144 ng/ml (=2,000 IU/ml) of PEG-IFN-α2a by apoptosis detection assay (Table 1). Non-pegylated IFN-α2a induced much more apoptosis than PEG-IFN-α2a.

Effects of PEG-IFN-α2a on HCC Cell Proliferation in Nude Mice

Chronological changes in estimated tumor volume after subcutaneous injection of cultured HAK-1B or KIM-1cells to nude mice are summarized in Figure 3. Dose-dependent suppression of tumor volume was observed in mice receiving PEG-IFN-α2a. In the experiment of HAK-1B tumors, a significant difference in the changes in tumor volume and tumor weight was observed between the Control mice and the mice

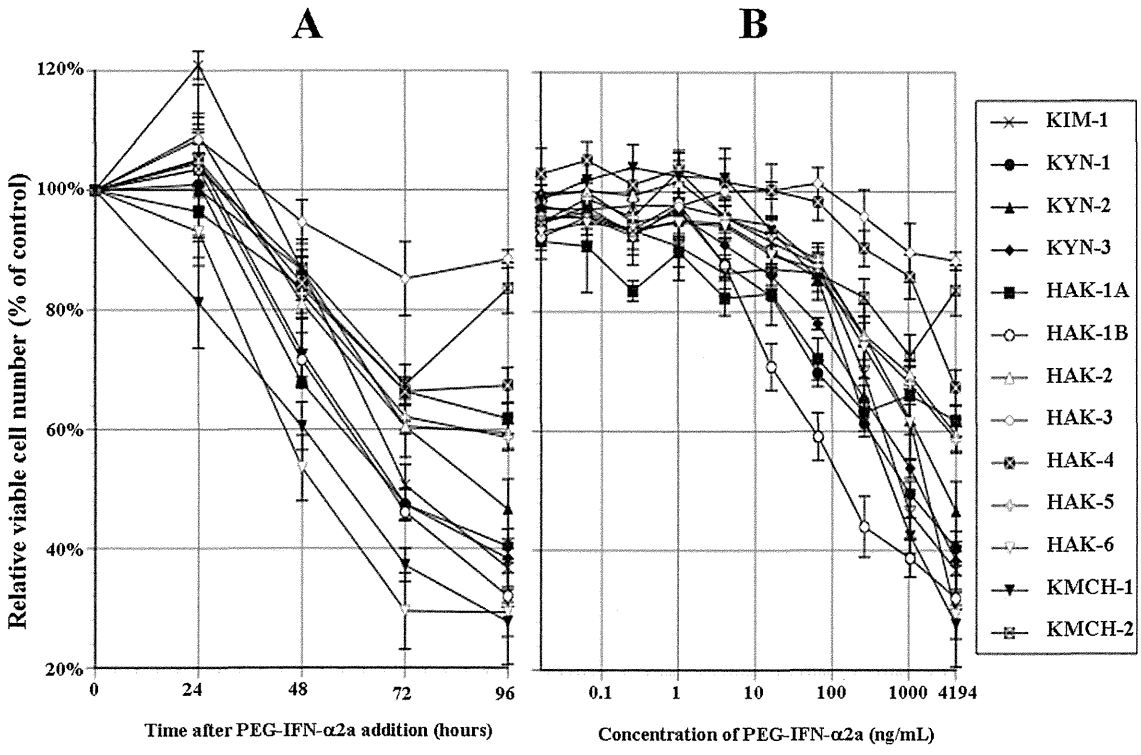

Figure 1. Anti-proliferative effect of PEG-IFN-α2a. (A) Chronological changes in relative viable cell number (% of the control) after adding 4,194 ng/mL of PEG-IFN-α2a. Growth was suppressed with time in 8 cell lines. (B) 96 hours after adding 10 different concentrations of PEG-IFN-α2a. Cell proliferation was suppressed in a dose-dependent manner in 11 cell lines. The suppression was significant ($P < 0.0001$~0.05) in the ranges of 0.016~4,194 ng/mL of PEG-IFN-α2a in HAK-6, 0.256~4,194 ng/mL in KYN-3 and HAK-1A, 4.096~4,194 ng/mL in KIM-1, KYN-1, HAK-1B, HAK-2 and KMCH-2, 16.4~4,194 ng/mL in KYN-2, HAK-5 and KMCH-1, 262~4,194 ng/mL in HAK-4, and at 4,194 ng/mL in HAK-3 (Student *t*-test). Eight samples were used in each experiment (n = 8). The experiment was repeated at least 3 times for each cell line. The figures represent average ± SE of the experiments.

doi: 10.1371/journal.pone.0083195.g001

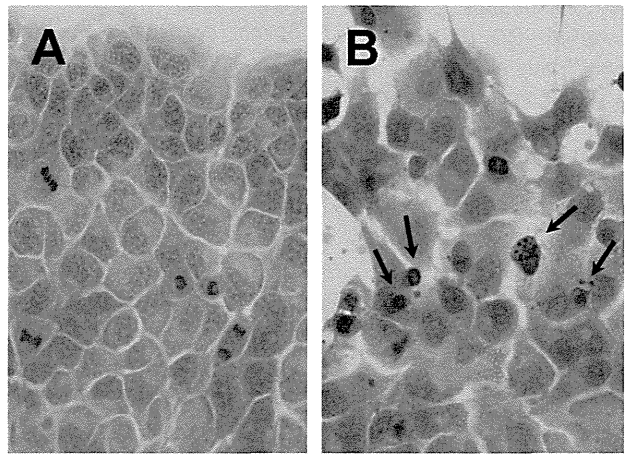

Figure 2. Photomicrograph of HAK-1B cells cultured for 72 hours on a Lab-Tek Chamber slide. (A) Without PEG-IFN-α2a in culture medium. (B) With 4,194 ng/mL of PEG-IFN-α2a in culture medium. Apoptotic cells (short arrows) characterized by cytoplasmic shrinkage, chromatic condensation and nuclear fragmentation were noted (HE staining, X 200).

doi: 10.1371/journal.pone.0083195.g002

Table 1. Quantitative analysis of apoptosis in HAK-1B or KIM-1.

	Annexin V-EGFP apoptotic cells (%)		
Cell line[a]	Control	IFN-α2a	PEG-IFN-α2a
HAK-1B	4.1 ± 0.5[b]	18.5 ± 0.3	10.9 ± 0.5
KIM-1	9.4 ± 0.4	47.0 ± 0.2	29.8 ± 2.1

[a] Cells were cultured with medium alone (Control), IFN-α2a (10 ng/ml=2,000 IU/ml) or PEG-IFN-α2a (144 ng/ml=2,000 IU/ml). [b] Mean ±SE.

doi: 10.1371/journal.pone.0083195.t001

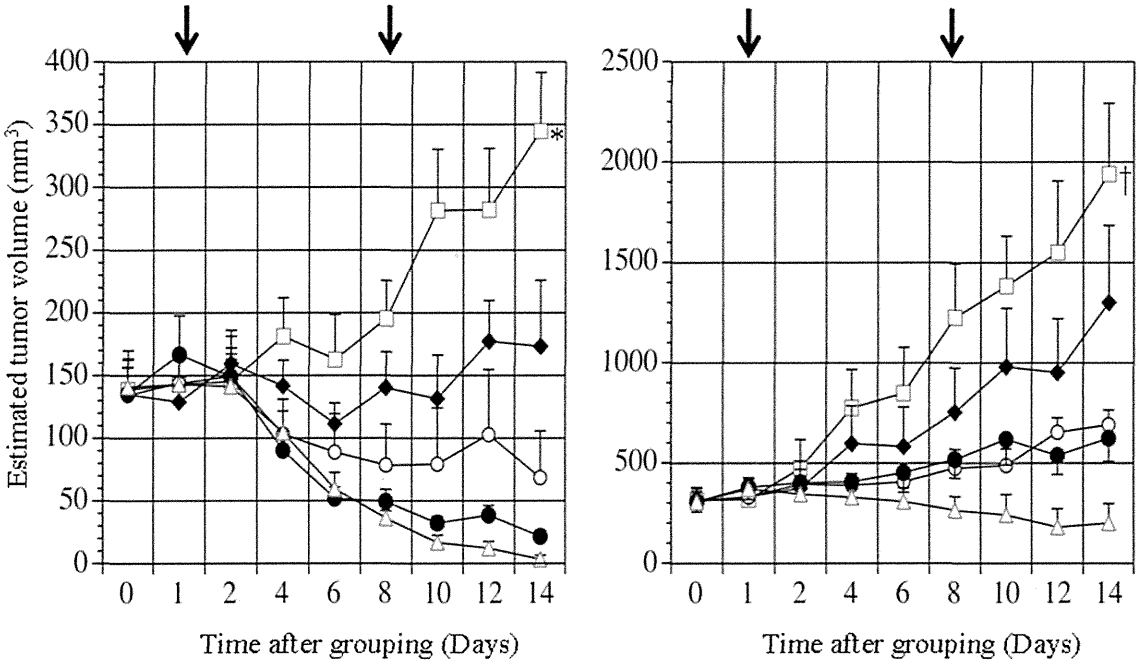

Figure 3. Time-course change in estimated tumor volumes of subcutaneously transplanted HAK-1B (A) or KIM-1 (B) tumors in nude mice in Experiment 1. The mice received a subcutaneous injection of 0.06 (▲), 0.6 (○), 6 (●), or 60 (Δ) μg of PEG-IFN-α2a, or medium alone (Control) (□), once a week for 2 consecutive weeks. The arrows show the days of injection. The figures represent average ± SE. *$P < 0.0001$, versus the other groups. †$P < 0.01$, versus the other groups.

doi: 10.1371/journal.pone.0083195.g003

that received 0.06, 0.6, 6 or 60 μg of PEG-IFN-α2a ($P < 0.0001$ by two-factor factorial ANOVA; and $P < 0.001$~0.02 by the Mann-Whitney U test, Figure 3A and Table 2). In the experiment of KIM-1 tumors, a significant reduction of tumor volume was also observed with the use of PEG-IFN-α2a ($P < 0.001$ by two-factor factorial ANOVA, Figure 3B). There were significant differences in the actual tumor weight between the Control group and the PEG-IFN-α2a groups, except for the PEG-IFN-α2a (0.06 μg) group (Table 2). The actual tumor weight at the end of the experiment 2 was summarized in Table 3. Subcutaneous injection of 0.6 μg of PEG-IFN-α2a induced the significant reduction of tumor weight, compared with the Control group and the group that received the same international unit of non-pegylated IFN-α2a ($P<0.005$ and $P<0.03$, respectively). In this experiment, there was no significant difference between the Control group and the PEG-IFN-α2a (0.06 μg) group ($P=0.078$).

Histological examination of the HAK-1B tumor specimens stained with HE revealed that the numbers of apoptotic cells in the mice treated with PEG-IFN-α2a (0.06 or 0.6 μg) were significantly higher than that of the Control, and the number increased dose dependently (Figure 4, A and B; Table 4). The incidence of apoptosis in TUNEL-stained sections showed the same tendencies as those obtained in HE-stained sections (Figure 4C and Table 4). Immunohistochemical examination of BrdU uptake in HAK-1B tumors revealed that there was no significant difference in BrdU labeling index between the Control and PEG-IFN-α2a (0.06 or 0.6 μg) groups (Table 4). As for apoptosis, similar findings were observed in experiment 2 in which KIM-1 was used. The group treated with 0.6 μg of PEG-IFN-α2a showed increased number of apoptotic cells than the control group. There was no significant difference between the control and IFN-α2a group. In addition, the group treated with

Table 2. The weight of subcutaneous tumors of HAK-1B or KIM-1 cells in nude mice at killing (Experiment 1).

	Tumor weight (g)	
Treatment group[a]	**HAK-1B**	**KIM-1**
Control	0.303 ± 0.05[b, c]	1.050 ± 0.24[e]
PEG-IFN-α2a (0.06 μg)	0.141 ± 0.03[d]	0.725 ± 0.17[f]
PEG-IFN-α2a (0.6 μg)	0.033 ± 0.01	0.439 ± 0.04
PEG-IFN-α2a (6 μg)	0.015 ± 0.01	0.434 ± 0.04
PEG-IFN-α2a (60 μg)	0.0	0.076 ± 0.05

[a] Cultured HAK-1B or KIM-1 cells (1.0 X 10^7) were subcutaneously transplanted into nude mice. Five groups of 8 mice received either phosphate-buffered saline (PBS) (Control) or PBS with the different dosages of PEG-IFN-α2a (0.06–60 μg) once a week. All mice were killed and the tumor weight was measured on the 15th day. [b] Mean ± SE. [c] $P < 0.02$, versus the PEG-IFN-α2a (0.06 μg) group; $P < 0.001$, versus the PEG-IFN-α2a (0.6 μg) group; $P < 0.001$, versus the PEG-IFN-α2a (6 μg) group. [d] $P < 0.02$, versus PEG-IFN-α2a (60 μg). [e] Not significant, versus the PEG-IFN-α2a (0.06 μg) group; $P < 0.03$, versus the PEG-IFN-α2a (0.6 μg) group; $P < 0.05$, versus the PEG-IFN-α2a (6 μg) group; $P < 0.01$, versus the PEG-IFN-α2a (60 μg) group. [f] $P < 0.05$, versus the PEG-IFN-α2a (60 μg) group.

doi: 10.1371/journal.pone.0083195.t002

Table 3. The actual weight and numbers of apoptotic cells of subcutaneous tumors at killing (Experiment 2).

Treatment group[a]	activity of interferon (IU)	Tumor weight (g)	Apoptosis (Number of cells/0.25mm^2)
Control	0 IU	0.726 ± 0.09[b, c]	7.6 ± 0.9[d]
IFN-α2a (0.0042 μg)	840 IU	0.588 ± 0.07[d]	7.9 ± 0.9[g]
IFN-α2a (0.042 μg)	8,400 IU	0.531 ± 0.04[e]	7.6 ± 0.7[h]
PEG-IFN-α2a (0.06 μg)	840 IU	0.493 ± 0.04[f]	8.9 ± 0.9
PEG-IFN-α2a (0.6 μg)	8,400 IU	0.355 ± 0.03	9.7 ± 1.0*

[a] Cultured HAK-1B cells (1.0 X 10^7) were subcutaneously transplanted into nude mice. Five groups of 8 mice received either PBS (Control), PBS with 0.0042 or 0.042 μg of IFN-α2a (840 or 8,400 IU, respectively), or PBS with 0.06 or 0.6 μg of PEG-IFN-α2a (840 or 8,400 IU, respectively). All mice were killed and the tumor weight was measured on the 15th day. The number of apoptotic cells was counted in at least three 0.25 mm^2-areas in each section stained with hematoxylin and eosin, and the average number per area in each group was obtained. [b] Mean ± SE. [c] $P < 0.005$, versus the PEG-IFN-α2a (0.6 μg) group. [d] $P < 0.02$, versus the PEG-IFN-α2a (0.6 μg) group. [e] $P < 0.03$, versus the PEG-IFN-α2a (0.6 μg) group. [f] $P < 0.02$, versus the PEG-IFN-α2a (0.6 μg) group. [g] $P < 0.05$, versus the PEG-IFN-α2a (0.6 μg) group. [h] $P < 0.001$, versus the PEG-IFN-α2a (0.6 μg) group.

doi: 10.1371/journal.pone.0083195.t003

0.6 μg of PEG-IFN-α2a (8,400 IU) showed higher number of apoptotic cells than those with 0.042 μg of IFN-α2a (8,400 IU).

The resected tumor of the PEG-IFN-α2a group showed granulation tissue at the middle of the tumor to various degrees (Figure 5). Arteries that appeared in the granulation tissue were excluded in blood vessel count within tumor. There was no significant difference in the number of blood vessels per unit area within the HAK-1B tumor and the expression of bFGF and IL-8 in the tumors between the PEG-IFN-α2a group and the Control group (Figure 5; Table 5).

Discussion

In the *in vitro* study, we showed that PEG-IFN-α2a inhibit the growth of 8 and 11 out of 13 cell lines in a time- and dose-dependent manner, however, PEG-IFN-α2a was apparently less active on an IC50 basis, compared with either PEG-IFN-α2b or IFN-α2b or consensus IFN-α or BALL-1 lymphoblastoid IFN-α which was tested in the same experimental condition in our previous reports [10,18,21]. For example, IC50 for HAK-1B cells was approximately 253 ng/ml of PEG-IFN-α2a, 13.1 ng/ml of PEG-IFN-α2b, 2.4 ng/ml of IFN-α2b, 0.7 ng/ml of consensus IFN-α and 1.1 ng/ml of BALL-1 lymphoblastoid IFN-α. On the other hand, in the *in vivo* study, s.c. injection of PEG-IFN-α2a once a week showed better antitumor effect on a tumor volume or weight basis, compared with that of non-pegylated IFN-α2a. These results might support our hypothesis that continuous contact with IFNs induces strong *in vivo* antitumor effects, and are not surprising because it was reported that PEG-IFN-α2a showed less active in vitro antiviral activity and but had much more *in vivo* antitumor activity than non-pegylated IFN-α2a [23]. We also showed that PEG-IFN-α2a can inhibit the proliferation of CHC cell lines as well as HCC. In MTT assay, the growth of KMCH-1 was well suppressed although another CHC cell line, KMCH-2 was not. One possible explanation for the different sensitivity between KMCH-1 and KMCH-2 is that the origin of KMCH-1 is CHC, classical type and that of KMCH-2 is CHC with stem-cell features, intermediate-cell subtype according to the latest WHO classification [24]. Such a stem-cell properties of the tumor might be the reason for IFN resistance. Another interesting finding in the *in vitro* study is the discrepancy between the results of MTT assay and apoptosis detection assay. When HAK-1B or KIM-1 was cultured with PEG-IFN-α2a, IC50 for HAK-1B was much lower than that for KIM-1 although HAK-1B showed lower rate of apoptotic cells than KIM-1. These findings suggest that there might be some

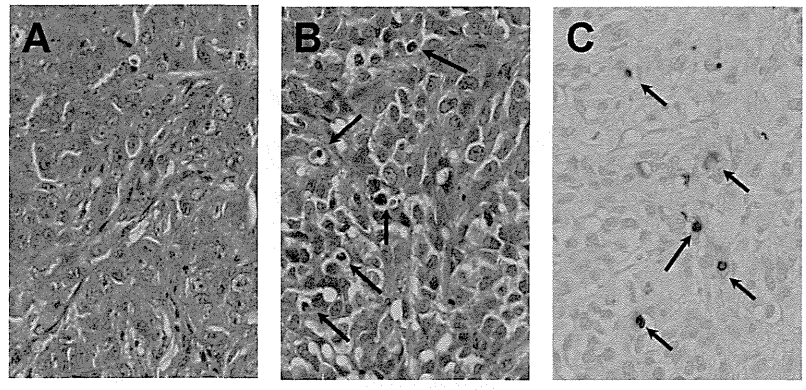

Figure 4. Photomicrograph of subcutaneous human HCC tumor in nude mice that was developed after the injection of HAK-1B cells. (A) A control mouse that received culture medium alone. The tumor shows a compact arrangement of tumor cells and a sinusoid-like structure in the stroma. (B) A mouse that received a s.c. injection of 0.06 μg of PEG-IFN-α2a. There are some apoptotic tumor-cells characterized by shrinkage and eosinophilic change in the cytoplasm, chromatin condensation and/or fragmentation of nuclei (arrows, HE staining, X200). (C) The same tumor as shown in (B). There are some TUNEL-positive cells showing brown nuclei (arrows, stained by the TUNEL technique, X200).

doi: 10.1371/journal.pone.0083195.g004

Table 4. Numbers of apoptotic cells and BrdU-positive cells in human HCC tumors subcutaneously transplanted in nude mice.

	Apoptosis[b] (Number of cells/0.25mm^2)		BrdU Labeling Index[c] (Number of positive cells/0.25mm^2)
Treatment group[a]	HE stain	TUNEL method	
Control	8.4 ± 0.8[d,e]	9.6 ± 1.1[e]	32.3 ± 1.6[f]
PEG-IFN-α2a (0.06 μg)	12.2 ± 1.0	15.4 ± 1.8	27.0 ± 2.6
PEG-IFN-α2a (0.6 μg)	12.4 ± 0.9	16.1 ± 1.5	31.3 ± 6.9

[a] Cultured HAK-1B cells (1.0 X 10^7) were subcutaneously transplanted into nude mice. Five groups of 8 mice received either phosphate-buffered saline (PBS) (Control) or PBS with the different dosages of PEG-IFN-α2a (0.06–60 μg) once a week. Tumors of mice that received 6 or 60 μg of PEG-IFN-α2a could not be used because the tumors were too small to evaluate. All mice were killed on the 15th day. [b] The number of apoptotic cells was counted in at least three 0.25 mm^2-areas in each section stained with hematoxylin and eosin, and the average number per area in each group was obtained. The number of TUNEL-positive cells was also counted in the same manner. [c] The number of BrdU-positive cells was counted in at least three 0.25 mm^2-areas in each section, and the average number per area in each group was obtained as the labeling index. [d] Mean ± SE. [e] $P < 0.02$, versus the other groups. [f]. Not significant, versus the other groups.

doi: 10.1371/journal.pone.0083195.t004

mechanisms other than apoptosis, which affect the sensitivity to antitumor effects of PEG-IFN-α2a. We previously reported that both pegylated and non-pegylated IFN-α inhibited the proliferation of cultured HCC cells by inducing the cell-cycle arrest [10,18]. The expression of interferon receptor on tumor cells might be a possible factor related to antitumor effect. For instance, Nagano et al reported that the expression of this type I IFN receptor on HCC tissue might be a useful predictor to find potential responder to INF-α/5-fluorouracil combination therapy [25]. Immunomodulation by IFNs has also been well studied as a factor related to antitumor effect. In this study, we used athymic mice, which lack mature T-cell, and human IFNs. Since IFNs are species-specific [26], we surmise that this immunomodulatory effect is limited in our study, but this should be confirmed in the future study using mouse IFN.

Morphological observation of the subcutaneous tumors of nude mice revealed that s.c. injection of PEG-IFN-α2a induce the significant increase of apoptotic cells compared with Control group. This result in the *in vivo* study is consistent with that in the *in vitro* study showing characteristic changes of apoptosis after adding PEG-IFN-α2a. Although the inhibition of angiogenesis as well as the induction of apoptosis is regarded as one of the biological effects of IFNs, there was no significant difference in the number of artery-like blood vessels of the subcutaneous tumors between the control and treatment groups. There are two possible explanations of this finding. Firstly, PEG-IFN-α2a was less effective for mouse endothelial cells compared with human cancer cells due to the species specificity of human IFNs. Secondly, it might be difficult to visualize the alteration in the number of vessels in order to examine the efficacy of drugs that possess antiangiogenic

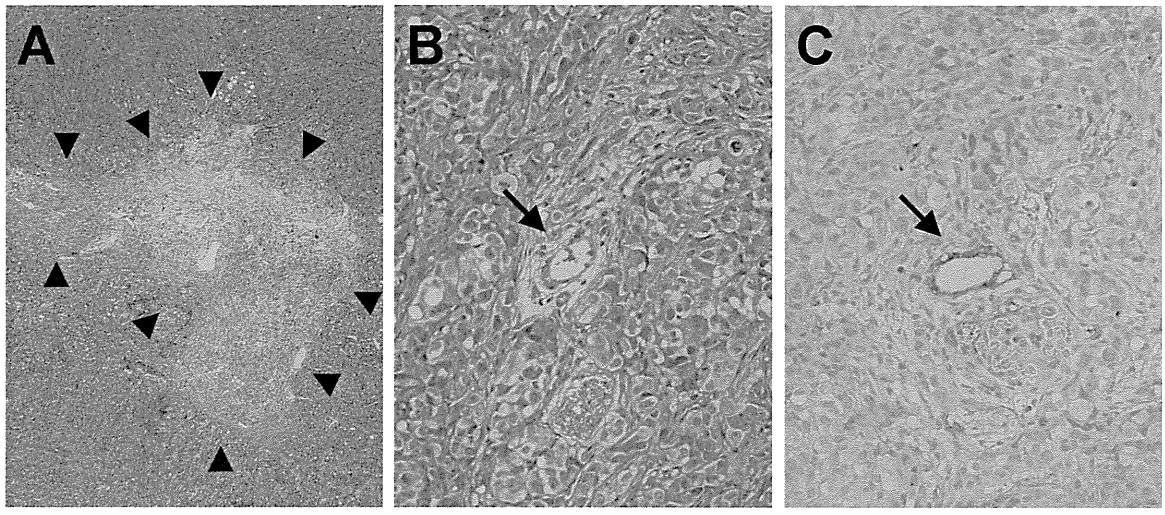

Figure 5. Photomicrograph of resected HAK-1B tumor. (A) Tumor cells are replaced with large granulation tissue at the middle of resected tumor. (arrowheads, HE staining, X20). (B) Artery-like blood vessels in the tumor (arrow, HE staining, X200). (C) Artery-like blood vessel in the tumor (arrow, CD34/α-SMA double-immunostain, X200).
doi: 10.1371/journal.pone.0083195.g005

Table 5. Numbers of artery-like blood vessels, and Enzyme-linked immunosorbent assay (ELISA) of angiogenesis factors in human HCC tumors subcutaneously transplanted in nude mice.

	Artery-like blood vessel[b] (Number of vessels/mm2)	Levels in the tumor lysate[c] (pg/40 μg cellular protein)	
Treatment group[a]	**Inside of tumor**	**bFGF**	**IL-8**
Control	0.104 ± 0.02[d,e]	14.0 ± 1.8[e]	2.8 ± 1.0[e]
PEG-IFN-α2a (0.06 μg)	0.194 ± 0.05	19.8 ± 2.1	4.9 ± 1.3

[a] Cultured HAK-1B cells (1.0 X 10^7) were subcutaneously transplanted into nude mice. Five groups of 8 mice received either phosphate-buffered saline (PBS) (Control) or PBS with the different dosages of PEG-IFN-α2a (0.06–60 μg) once a week. Tumors of mice that received 0.6, 6 or 60 μg of PEG-IFN-α2a could not be used because the tumors were too small to evaluate. All mice were killed on the 15th day. [b] The number of artery-like blood vessels within tumor was counted on each section, and the average number per area in each group was obtained. [c] The expression levels of basic fibroblast growth factor (bFGF) and IL-8 of the resected tumors were measured by ELISA. [d] Mean ± SE. [e]. Not significant, versus the PEG-IFN-α2a (0.06 μg) group.
doi: 10.1371/journal.pone.0083195.t005

activity. Hlatky et al explained in their review article that the reason is that the tightness of the coupling between vessel drop-out and tumor-cell drop-out after the treatment is different [27]. We had observed similar findings in our previous report in which human HCC tumors subcutaneously transplanted in nude mice showed much apoptosis in either PEG-IFN-α2b or IFN-α2b treatment group compared with the Control group, but no significant difference in the number of blood vessels [10]. Kojiro et al also showed that s.c. injection of BALL-1 lymphoblastoid IFN-α increase the number of artery-like blood vessels and the protein expression of bFGF within HCC xenograft tumors in spite of the significant decrease of actual tumor weight [28]. In contrast, Dinney et al showed that IFN-α2a decreases the blood vessel density and the expression of bFGF in orthotopic xenograft model of bladder tumor [29]. The reason for these contrary findings remains unclear and further evaluation with caution is needed by using different doses and types of IFNs and different cell lines, not only in subcutaneous tumor model but also in orthotopic model.

The association between IFN therapy and occurrence or recurrence of HCC has been investigated in some reports. HALT-C trial group showed in their randomized control trial in a large cohort that long-term PEG-IFN-α2a therapy does not reduce the incidence of HCC among patients with chronic HCV infection who have previously failed to achieve a sustained virologic response to therapy [30]. Among only patients with cirrhosis, long-term PEG-IFN-α2a therapy reduced a risk of HCC after a long-time observation [31]. EPIC study group also showed long-term PEG-IFN-α2b therapy does not prevent HCC [32]. On the other hand, Nishiguchi et al reported that long-term IFN-α therapy after curative resection of HCV-related HCC prolongs the survival rate, although preventive effect of intrahepatic recurrence was marginal [33]. Sakaguchi et al also showed that among patients who underwent radical

radiofrequency therapy for HCV-related HCC, long-term IFN-α2b therapy reduced the recurrent rate of HCC [4]. These reports with conflicting results may be suggesting that IFN therapy is effective only after the initial curative treatment of HCV-related HCC. In addition, there are several reports that support that IFN therapy prevents the development of HCC among patients with chronic HBV infection or those underwent curative resection of HBV-related HCC [5,7]. Thus the chemopreventive effect of IFNs against HCC are still controversial, and mechanisms behind that remain unclear. Antiviral effect against HBV and HCV, which are risk factors for HCC, and immunomodulatory effect of IFNs are regarded as main mechanisms. Another possible mechanism is that IFNs may suppress the growth of clinically undetectable HCC due to their direct antitumor effect. Our finding in the current study provide the evidence that PEG-IFN-α2a possesses the direct antitumor effect against HCC.

In conclusion, we demonstrated antitumor effect of PEG-IFN-α2a for human liver cancer cells *in vitro* and *in vivo* and our results suggest that longer contact to IFNs may induce stronger antitumor effect in body. PEG-IFN-α2a might be a possible treatment option for HCC as well as chronic viral hepatitis. Further studies are needed from both molecular and clinical view points in order to find out particular patient group those respond to this therapy.

Acknowledgements

We thank Ms. Akemi Fujiyoshi for her assistance in our experiments.

Author Contributions

Conceived and designed the experiments: HK JA SO ON HY. Performed the experiments: HK JA SO SS MY MN KU KU TK KT YU ON HY. Analyzed the data: HK JA SO SS MY MN KU KU TK KT YU ON HY. Contributed reagents/materials/analysis tools: HK JA SO SS MY MN KU KU TK KT YU ON HY. Wrote the manuscript: HK JA SO ON HY.

References

1. Pestka S, Langer JA, Zoon KC, Samuel CE (1987) Interferons and their actions. Annu Rev Biochem 56: 727–777. doi:10.1146/annurev.bi.56.070187.003455. PubMed: 2441659.
2. Jonasch E, Haluska FG (2001) Interferon in oncological practice: review of interferon biology, clinical applications, and toxicities. Oncologist 6: 34–55. doi:10.1634/theoncologist.6-1-34. PubMed: 11161227.
3. Lai CL, Lau JY, Wu PC, Ngan H, Chung HT et al. (1993) Recombinant interferon-alpha in inoperable hepatocellular carcinoma: a randomized controlled trial. Hepatology. 17: 389-394. doi:10.1002/hep.1840170307. PubMed: 8383088.
4. Sakaguchi Y, Kudo M, Fukunaga T, Minami Y, Chung H et al. (2005) Low-dose, long-term, intermittent interferon-alpha-2b therapy after radical treatment by radiofrequency ablation delays clinical recurrence in patients with hepatitis C virus-related hepatocellular carcinoma. Intervirology 48: 64–70. doi:10.1159/000082097. PubMed: 15785092.
5. Miyake Y, Kobashi H, Yamamoto K (2009) Meta-analysis: the effect of interferon on development of hepatocellular carcinoma in patients with chronic hepatitis B virus infection. J Gastroenterol 44: 470–475. doi: 10.1007/s00535-009-0024-z. PubMed: 19308310.
6. Miyake Y, Iwasaki Y, Yamamoto K (2010) Meta-analysis: reduced incidence of hepatocellular carcinoma in patients not responding to interferon therapy of chronic hepatitis C. Int J Cancer 127: 989–996. PubMed: 19957327.
7. Qu LS, Jin F, Huang XW, Shen XZ (2010) Interferon-α therapy after curative resection prevents early recurrence and improves survival in patients with hepatitis B virus-related hepatocellular carcinoma. J Surg Oncol 102: 796–801. doi:10.1002/jso.21741. PubMed: 20886584.
8. Manns MP, McHutchison JG, Gordon SC, Rustgi VK, Shiffman M et al. (2001) Peginterferon alfa-2b plus ribavirin compared with interferon alfa-2b plus ribavirin for initial treatment of chronic hepatitis C: a randomised trial. Lancet 358: 958–965. doi:10.1016/S0140-6736(01)06102-5. PubMed: 11583749.
9. Fried MW, Shiffman ML, Reddy KR, Smith C, Marinos G et al. (2002) Peginterferon alfa-2a plus ribavirin for chronic hepatitis C virus infection. N Engl J Med 347: 975–982. doi:10.1056/NEJMoa020047. PubMed: 12324553.
10. Yano H, Ogasawara S, Momosaki S, Akiba J, Kojiro S et al. (2006) Growth inhibitory effects of pegylated IFN alpha-2b on human liver cancer cells *in vitro* and *in vivo*. Liver Int 26: 964–975. doi:10.1111/j.1478-3231.2006.01321.x. PubMed: 16953837.
11. Utsunomiya I, Iemura A, Yano H, Akiba J, Kojiro M (1999) Establishment and characterization of a new human hepatocellular carcinoma cell line, HAK-3, and its response to growth factors. Int J Oncol 15: 669–675. PubMed: 10493947.
12. Murakami T (1984) Establishment and characterization of human hepatoma cell line (KIM-1). Acta Hepatol Jpn 25: 532–539. doi: 10.2957/kanzo.25.532.
13. Murakami T, Maruiwa M, Fukuda K, Kojiro M, Tanaka M, et al. (1988) Characterization of a new human hepatoma cell line (KYN-3) derived from the ascites of the hepatoma patient [Abstract]. Jpn J Cancer Res 292 Proceedings of the Japanese Cancer Association
14. Murakami T, Yano H, Maruiwa M, Sugihara S, Kojiro M (1987) Establishment and characterization of a human combined hepatocholangiocarcinoma cell line and its heterologous transplantation in nude mice. Hepatology 7: 551–556. doi:10.1002/hep.1840070322. PubMed: 3032760.
15. Haramaki M, Yano H, Iemura A, Momosaki S, Ogasawara S et al. (1997) A new human hepatocellular carcinoma cell line (HAK-2) forms various structures in collagen gel matrices. Hum Cell 10: 183–192. PubMed: 9436038.
16. Yano H, Iemura A, Fukuda K, Mizoguchi A, Haramaki M et al. (1993) Establishment of two distinct human hepatocellular carcinoma cell lines from a single nodule showing clonal dedifferentiation of cancer cells. Hepatology 18: 320–327. doi:10.1016/0270-9139(93)92802-7. PubMed: 8393423.
17. Yano H, Iemura A, Haramaki M, Momosaki S, Ogasawara S et al. (1996) A human combined hepatocellular and cholangiocarcinoma cell line (KMCH-2) that shows the features of hepatocellular carcinoma or cholangiocarcinoma under different growth conditions. J Hepatol 24: 413–422. doi:10.1016/S0168-8278(96)80161-9. PubMed: 8738727.
18. Yano H, Iemura A, Haramaki M, Ogasawara S, Takayama A et al. (1999) Interferon alfa receptor expression and growth inhibition by interferon alfa in human liver cancer cell lines. Hepatology 29: 1708–1717. doi:10.1002/hep.510290624. PubMed: 10347112.
19. Yano H, Kojiro M, Nakashima T (1986) A new human hepatocellular carcinoma cell line (KYN-1) with a transformation to adenocarcinoma. In Vitro Cell Dev Biol 22: 637–646. doi:10.1007/BF02623477. PubMed: 2430933.
20. Yano H, Maruiwa M, Murakami T, Fukuda K, Ito Y et al. (1988) A new human pleomorphic hepatocellular carcinoma cell line, KYN-2. Acta Pathol Jpn 38: 953–966. PubMed: 2847482.
21. Hisaka T, Yano H, Ogasawara S, Momosaki S, Nishida N et al. (2004) Interferon-αCon1 suppresses proliferation of liver cancer cell lines *in vitro* and *in vivo*. J Hepatol 41: 782–789. doi:10.1016/j.jhep.2004.07.012. PubMed: 15519651.
22. Takemoto Y, Yano H, Momosaki S, Ogasawara S, Nishida N et al. (2004) Antiproliferative effects of interferon-alphaCon1 on ovarian clear cell adenocarcinoma *in vitro* and *in vivo*. Clin Cancer Res 10: 7418–7426. doi:10.1158/1078-0432.CCR-04-0279. PubMed: 15534119.
23. Bailon P, Palleroni A, Schaffer CA, Spence CL, Fung WJ et al. (2001) Rational design of a potent, long-lasting form of interferon: a 40 kDa branched polyethylene glycol-conjugated interferon alpha-2a for the treatment of hepatitis C. Bioconjug Chem 12: 195-202. doi:10.1021/bc000082g. PubMed: 11312680.

24. Bosman FT, Carneiro F, Hruban RH, Theise ND (2010) WHO Classification of Tumours of the Digestive System (4th Revised edition). Lyon, France, IARC Press. pp. 225-227.
25. Nagano H, Miyamoto A, Wada H, Ota H, Marubashi S et al. (2007) Interferon-alpha and 5-fluorouracil combination therapy after palliative hepatic resection in patients with advanced hepatocellular carcinoma, portal venous tumor thrombus in the major trunk, and multiple nodules. Cancer 110: 2493–2501. doi:10.1002/cncr.23033. PubMed: 17941012.
26. Gillespie G, Carter WA (1981-1982) Species specificity of interferon. Tex Rep Biol Med 41: 37-42. PubMed: 6184826.
27. Hlatky L, Hahnfeldt P, Folkman J (2002) Clinical application of antiangiogenic therapy: microvessel density, what it does and doesn't tell us. J Natl Cancer Inst 94: 883-893. doi:10.1093/jnci/94.12.883. PubMed: 12072542.
28. Kojiro S, Yano H, Ogasawara S, Momosaki S, Takemoto Y et al. (2006) Antiproliferative effects of 5-fluorouracil and interferon-alpha in combination on a hepatocellular carcinoma cell line *in vitro* and *in vivo*. J Gastroenterol Hepatol 21: 129–137. doi:10.1111/j.1440-1746.2005.04154.x. PubMed: 16706824.
29. Dinney CP, Bielenberg DR, Perrotte P, Reich R, Eve BY et al. (1998) Inhibition of basic fibroblast growth factor expression, angiogenesis, and growth of human bladder carcinoma in mice by systemic interferon-alpha administration. Cancer Res 58: 808–814. PubMed: 9485039.
30. Di Bisceglie AM, Shiffman ML, Everson GT, Lindsay KL, Everhart JE et al. (2008) Prolonged therapy of advanced chronic hepatitis C with low-dose peginterferon. N Engl J Med 359: 2429–2441. doi:10.1056/NEJMoa0707615. PubMed: 19052125.
31. Lok AS, Everhart JE, Wright EC, Di Bisceglie AM, Kim HY et al. (2011) Maintenance peginterferon therapy and other factors associated with hepatocellular carcinoma in patients with advanced hepatitis C. Gastroenterology 140: 840–849. doi:10.1053/j.gastro.2010.11.050. PubMed: 21129375.
32. Bruix J, Poynard T, Colombo M, Schiff E, Burak K et al. (2011) Maintenance therapy with peginterferon alfa-2b does not prevent hepatocellular carcinoma in cirrhotic patients with chronic hepatitis C. Gastroenterology 140: 1990–1999. doi:10.1053/j.gastro.2011.03.010. PubMed: 21419770.
33. Nishiguchi S, Tamori A, Kubo S (2005) Effect of long-term postoperative interferon therapy on intrahepatic recurrence and survival rate after resection of hepatitis C virus-related hepatocellular carcinoma. Intervirology 48: 71–75. doi:10.1159/000082098. PubMed: 15785093.

Original Research

Comparison Between T1 Relaxation Time of Gd-EOB-DTPA-Enhanced MRI and Liver Stiffness Measurement of Ultrasound Elastography in the Evaluation of Cirrhotic Liver

Masahiro Okada, MD, PhD,[1]* Takamichi Murakami, MD, PhD,[1] Norihisa Yada, MD, PhD,[2] Kazushi Numata, MD, PhD,[3] Minori Onoda, RT,[1] Tomoko Hyodo, MD, PhD,[1] Tatsuo Inoue, MD, PhD,[2] Kazunari Ishii, MD, PhD,[1] and Masatoshi Kudo, MD, PhD[2]

Purpose: To compare four imaging approaches in cirrhotic estimation; pre-enhancement T1 relaxation time (T1RT), reduction rate (RR) of T1RT, signal-based liver-to-muscle ratio (*L/M ratio*) on gadolinium ethoxybenzyl diethylenetriaminepentaacetic acid (Gd-EOB-DTPA)-enhanced magnetic resonance imaging (MRI), and liver stiffness measurement (LSM) of US elastography.

Materials and Methods: Consecutive 58 patients with chronic liver diseases who underwent both Gd-EOB-DTPA-enhanced MRI and FibroScan were analyzed. Four imaging approaches were evaluated by fibrosis score from liver biopsy and receiver operating characteristic (ROC) analysis.

Results: RR was found to be inversely correlated with LSM ($r=-0.65$). RR decreased with degree of fibrosis (F0-F1, $58.5\pm6.2\%$, versus F2-F3-F4, $48.8\pm11.7\%$, $P=0.010$, F0-F1-F2, $58.2\pm6.2\%$ versus F3-F4, $45.5\pm12.3\%$, $P=0.010$ and F0-F1, $58.5\pm6.2\%$, versus F2-F3, $52.1\pm12.0\%$, $P=0.0038$). LSM increased with degree of fibrosis (F0-F1, 5.4 ± 2.2 kPa versus F2-F3-F3, 19.3 ± 15.5 kPa, $P=0.0011$ and F0-F1-F2, 6.8 ± 3.6 kPa versus F3-F4, 23.8 ± 17.1 kPa, $P=0.0029$ and F0-F1, 5.4 ± 2.2 kPa, versus F2-F3, 11.4 ± 7.2 kPa, $P=0.0098$). Area under ROC curves were 0.83 (F3-F4), 0.72 (F2-F3-F4), 0.68 (F2-F3) for RR and 0.83 (F3-F4), 0.88 (F2-F3-F4), 0.81 (F2-F3) for LSM in discriminating between patients with fibrosis.

Conclusion: The capability by LSM was better than those by RR of T1RT, pre-enhancement T1RT, and L/M ratio to differentiate $F\geq2$, but LSM and RR of T1RT showed the same value to differentiate $F\geq3$.

Key Words: Gd-EOB-DTPA; MRI; US; liver fibrosis; elastography; T1 relaxation time
J. Magn. Reson. Imaging 2013;00:000–000.

HEPATIC FIBROSIS and cirrhosis represent a major public health problem worldwide. Progressive hepatic fibrosis leads to cirrhosis. Liver fibrosis leads to distinct alterations of the hepatic microvasculature, thus increased total hepatic vascular resistance. Early cirrhosis can be reversed by suppression of the fibrotic response (1,2). Common causes of liver cirrhosis are hepatitis C virus (HCV), hepatitis B virus (HBV), alcohol consumption, and nonalcoholic steatohepatitis (NASH). In patients with hepatitis C, progression of hepatic fibrosis is more rapid in those infected at an older age and increases with duration of infection (3).

Routine biochemical and hematological tests fail to quantify liver fibrosis in approximately 50% of patients (4). Liver biopsy is the gold standard in the assessment of liver fibrosis grade. Biopsy involves taking a fraction (~1/50,000th) of the total mass of the liver (5). However, liver biopsy has several limitations including physical discomfort due to its invasive nature. In addition, procedure-related complications such as bleeding (intrahepatic hematoma occurs in up to 6% of patients), bile leak, and pneumothorax can result from liver biopsy, although rare (6).

Ultrasound (US) elastography (7,8) is receiving increasing attention, because there is a need for alternative noninvasive methods to estimate the stage of liver fibrosis. This technology for quantitatively assessing hepatic stiffness has been introduced in the last several years. Liver stiffness measured using US elastography (FibroScan; Echosens, Paris, France) has been validated in the assessment of fibrosis in patients with chronic hepatitis (9). Transient

[1]Department of Radiology, Kinki University Faculty of Medicine, Osaka, Japan.
[2]Department of Gastroenterology and Hepatology, Kinki University Faculty of Medicine, Osaka, Japan.
[3]Gastroenterological Center, Yokohama City University Medical Center, Yokohama, Japan.
*Address reprint requests to: M.O., Kinki University Faculty of Medicine, Department of Radiology, 377-2 Ohno-Higashi, Osaka-Sayama, Osaka 589-8511, Japan. E-mail: mokada@gaia.eonet.ne.jp
Received March 7, 2013; Accepted November 18, 2013.
DOI 10.1002/jmri.24529
View this article online at wileyonlinelibrary.com.

elastography is widely available, noninvasive, and shows high accuracy in staging hepatic fibrosis. However, US elastography is not carried out on patients with ascites and narrow intercostal spaces.

Gadolinium ethoxybenzyl diethylenetriaminepentaacetic acid (Gd-EOB-DTPA) is a relatively new liver-specific contrast agent on magnetic resonance imaging (MRI). Gd-EOB-DTPA is gradually taken into hepatocyte cells, resulting in signal enhancement on T1-weighted images. This contrast agent is used substantially for the detection of HCC and liver metastasis on MRI (10–13), but it also has the potential to enable functional imaging with a T1 shortening effect at the hepatobiliary phase (14–19). The measurement of the T1 relaxation time (T1RT) of liver parenchyma before and after Gd-EOB-DTPA administration allows quantitative evaluation of Gd-EOB-DTPA uptake by the liver parenchyma. T1 mapping of the liver shows the distribution of T1RT in the liver, and is useful to recognize regional or whole liver function. On the other hand, signal-based measurement on MRI is widely used for the quantification to estimate degree of liver parenchymal enhancement.

It had been reported that it was possible to assess the staging of liver fibrosis using a rat NASH model by evaluating the signal intensity-time profile after Gd-EOB-DTPA injection (15). However, the potential of using this approach to assess the staging of liver fibrosis in human has not yet been assessed. The aim of the present study was to compare four imaging approaches in liver fibrosis estimation using a quantitative parameter for the classification of fibrosis, namely, pre-enhancement T1RT, T1RT and signal-based liver-to-muscle ratio on Gd-EOB-DTPA-enhanced MRI, and liver stiffness measurement (LSM) of US elastography (FibroScan).

MATERIALS AND METHODS

Patients

The Institutional Review Board of our university hospital approved the study, and all patients received informed consent forms for approval of the MR imaging, FibroScan, and liver biopsies. The inclusion criteria were as follows: chronic HCV infection; chronic HBV infection; clinical evidence for liver cirrhosis; and NASH. The exclusion criteria were cases complicated with other liver diseases or HCC. No patients had a past history of cardiac diseases that may produce image artifact by an irregular heartbeat interval.

Both Gd-EOB-DTPA-enhanced MR examination and FibroScan were performed on 63 consecutive patients (36 men and 27 women) with chronic liver disease. Patients had a mean age of 66 years (range 37–83 years).

MRI

A clinically available 3.0 T system (Achieva; Philips Medical System, Best, Netherlands) with a 6- or 32-channel phased-array surface coil was used. The Philips Research Integrated Development Environment (PRIDE) T1 fitting tool was employed for measurement of T1RT using data from the Look-Locker echo-planar imaging sequence (T1 mapping), which was addressed previously (16). Look-Locker-Turbo-Field-Echo (LL-TFE) sequences (repetition time, 12 msec; echo time, 1.7 msec; flip angle, 7°; field of view, 420 × 285 mm; zero-fill interpolation (zip), matrix; 112 × 66 (reconstruction 256 × 256); thickness, 10 mm; acquisition time, 1 phase = 145 msec, 31 phases; and acceleration factor, 2) were obtained before and 18 minutes after 0.025 mmol/kg of Gd-EOB-DTPA (Primovist: Bayer Schering Pharma, Berlin, Germany) administration. The T1 mapping image was obtained as a single axial slice.

Our routine MR examination sequences on Gd-EOB-DTPA-enhanced MRI were T1-weighted images with in-phase and opposed-phase at pre-enhancement, 3D T1-weighted image of arterial phase, portal venous phase, respiratory-triggered T2-weighted image with fat saturation, diffusion-weighted image with low and high b factors after contrast, 3D T1-weighted image approximately 20% minutes after injection (hepatobiliary phase). The 3D T1-weighted image was obtained as T1 high-resolution isotropic volume examination (THRIVE) with fat suppression; repetition time, 3.5 msec; echo time, 1.7 msec; flip angle, 10°; field of view, 350 × 350 mm; matrix, 320 × 256; thickness, 3 mm; and reduction factor, 2). All patients received Gd-EOB-DTPA administered at 2 mL/s through an intravenous line placed in a cubital vein and flushed with 32–36 mL of 0.9% saline at the same speed. This series on Gd-EOB-DTPA-enhanced MRI was performed as a routine clinical examination to detect and characterize liver tumors.

Analysis Using Gd-EOB-DTPA-Enhanced MRI

Gd-EOB-DTPA-enhanced MRI was performed for 63 patients. In these patients, T1RT and signal-based liver to paraspinal muscle ratio (L/M ratio) were independently measured by two examiners (M.O. and M.O.) Three regions of interest (ROIs) with a range of 50–60 pixels were placed manually in the liver (liver segments of 2/3, 5, and 6/7 using Couinaud's classification), avoiding visible intrahepatic vessels on T1 mapping images and 3D T1-weighted image obtained before and 18 minutes (20 minutes) after Gd-EOB-DTPA administration. The reason why 18 minutes after Gd-EOB-DTPA administration applied is because T1RT at 18 minutes after Gd-EOB-DTPA injection has possibilities to differentiate between patients with different liver dysfunction (16). Avoiding visible intrahepatic vessels on T1 mapping images was performed in reference to 3D T1-weighted image (hepatobiliary phase) because this study was planned to measure the liver parenchymal T1 relaxation time. Mean T1RT and liver signal of the L/M ratio for the three ROIs in segments of 2/3, 5, and 6/7 were considered representative hepatic T1RT and liver signal. First, pre-enhancement T1RT was measured to analyze whether there were differences between different grades of liver fibrosis. Second, the reduction rate (RR) of the T1RT

and increasing rate (IR) of the L/M ratio of the liver parenchyma were defined as follows:

$$\text{RR of the T1RT} = [(\text{T1pre} - \text{T1post})/\text{T1pre}] \times 100\%$$

where T1pre is T1RT at pre-enhancement and T1post is T1RT at post-enhancement (18 min).

$$\text{IR of the L/M ratio} = [(\text{L/M ratio post} - \text{L/M ratio pre})/\text{L/M ratio pre}] \times 100\%$$

where L/M ratio pre is L/M ratio at pre-enhancement and L/M ratio post is L/M ratio at post-enhancement (20 min); signal of muscle was obtained for the two ROIs on the left and right paraspinal muscle and was averaged.

Analysis Using US Elastography (FibroScan)

FibroScan was performed for 63 patients by one examiner (one hepatologist with 3 years of experience in US elastography). The LSM was obtained with the right intercostal approach. The principle of elastography using FibroScan has been described elsewhere (20,21). FibroScan measured the stiffness of the liver parenchyma using both US (5 MHz) and low-frequency (50 Hz) elastic waves from an ultrasound vibrator applied to the body wall. The results expressed in kPa after 10 validated measurements were performed at a depth of 25–45 mm from the skin surface. The interquartile range (IQR) of the FibroScan was recorded to assess the reproducibility of measured results (a smaller IQR is sensitive to the FibroScan measurements).

Pathological Diagnosis and Quantification of the Liver

Fifty-eight patients received liver biopsy by one examiner (a hepatologist with 10 years of experience in liver biopsy). In all patients, the intercostal approach was used for biopsy and the biopsy was performed at liver segment 5 of Couinaud's classification. To ensure accurate histological grading of liver fibrosis using US-guided needle core biopsy, at least two samples were taken from each patient's liver using an 18G needle (MONOPTY, C.R. Bard, Murray Hill, NJ) under local anesthesia. The liver biopsy specimen was fixed in formalin and embedded in paraffin. For liver fibrosis staging, hematoxylin and eosin and Masson's trichrome stains were used.

Liver fibrosis was scored using New Inuyama Classification, which involved the use of a five-grade scale (F0–F4) (22). Experienced pathologists (two pathologists with more than 10 years of experience in liver pathology) diagnosed the stage of liver fibrosis by consensus. This system was used to grade histological lesions by means of two separate scores, one for fibrosis (F) and the other for necroinflammation (activity). The fibrosis score was defined as: F0 = no fibrosis; F1 = fibrous portal expansion; F2 = bridging fibrosis (portal-portal or portal-central linkage); F3 = bridging fibrosis with lobular distortion (disorganization); and F4 = cirrhosis.

Statistical Analysis

Data from pre-enhancement T1RT, signal-based L/M ratio, T1RT on Gd-EOB-DTPA-enhanced MRI, and LSM of FibroScan were expressed as the mean ± standard deviation (SD). In order to assess the agreement between the two observers' measurements, simple regression analysis and Bland–Altman analysis between the two measurements by two observers for pre-enhancement T1RT, RR of the T1RT, and IR of the L/M ratio in the liver parenchyma were evaluated. The strength of the correlation between the RR of the T1RT in the liver parenchyma and the LSM obtained using the FibroScan was evaluated using simple regression analysis. The diagnostic performance and the linear combination of pre-enhancement T1RT, RR of the T1RT, IR of the L/M ratio, and LSM were assessed using the receiver operating characteristic (ROC) curve, which is a plot of sensitivity versus specificity. The area under the ROC curve (AUC) and the cutoff value were obtained by ROC analysis. Statistical analyses were performed using a commercially available Excel software (Microsoft Excel 2007; Microsoft, Tokyo, Japan), StatFlex v. 6.0 software (Artech, Osaka, Japan) and free statistical software "R" (R, v. 2.6.1; The R Project for Statistical Computing; http://www.r-project.org/). $P < 0.05$ was considered statistically significant.

RESULTS

Patients

In 63 patients with Gd-EOB-DTPA-enhanced MRI and FibroScan, FibroScan had unsuccessful measurements due to ascites, obesity, and narrow intercostal space in four patients and Gd-EOB-DTPA-enhanced MRI had misregistration of liver scan in one patient. Thus, pre-enhancement T1RT, signal-based L/M ratio, RR of T1RT, and LSM of FibroScan were compared in the remaining 58 patients (34 men and 24 women) with liver biopsy (Fig. 1 shows a T1 mapping in a patient with chronic hepatitis C and F1 of New Inuyama Classification). Chronic liver diseases were nonalcoholic fatty liver disease (NAFLD; $n = 25$), chronic hepatitis C ($n = 15$), chronic hepatitis B ($n = 4$), NASH ($n = 3$), alcoholic liver disease ($n = 2$), and liver cirrhosis ($n = 9$). There were Grade A ($n = 42$), Grade B ($n = 15$), and Grade C ($n = 1$) by Child-Pugh Classification in 58 patients.

The distribution of these scores for fibrosis were as follows: F0, $n = 13$; F1, $n = 14$; F2, $n = 12$; F3, $n = 10$; and F4, $n = 9$.

Agreement Between the Two observers' Measurements

Simple regression analysis and Bland–Altman analysis showed narrow limits of agreement between two observers' measurements of pre-enhancement T1RT,

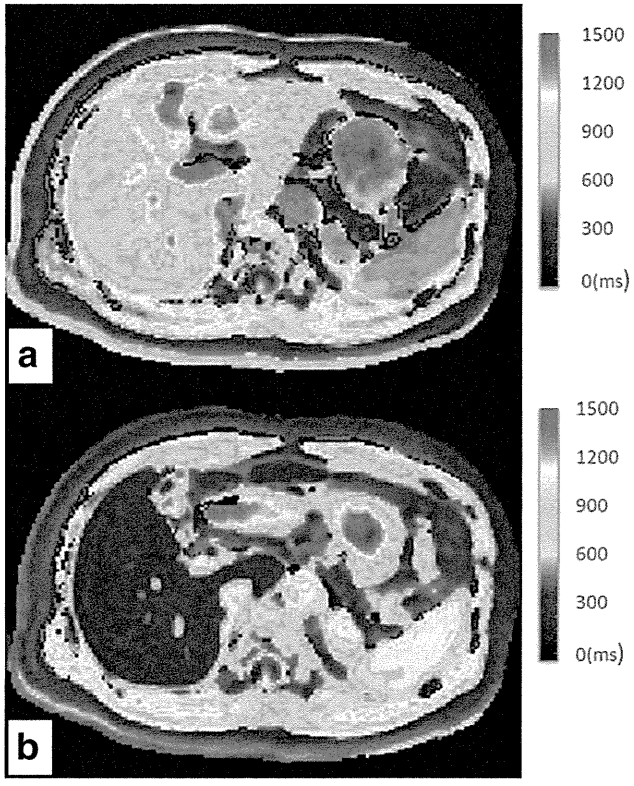

Figure 1. T1 mapping of a 64-year-old man (New Inuyama Classification: F1) with chronic HCV infection on Gd-EOB-DTPA-enhanced MRI. **a:** Pre-enhancement T1 mapping. Number in the right upper corner shows the scale of T1 relaxation time (T1RT). Mean T1RT for the three ROIs in segments of 2/3, 5, and 6/7 is considered representative T1RT for the liver. Pre-enhancement mean T1RT was 782.0 msec. **b:** Post-enhancement T1 mapping at 18 minutes. Number in the right upper corner shows the scale of T1RT. Mean T1RT for the three ROIs is considered representative T1RT for the liver. Mean T1RT at 18 minutes after enhancement was 256.2 msec. Thus, the reduction rate (RR = [(T1pre – T1post) / T1pre] × 100%) of the T1RT of liver parenchyma is 67.2%.

RR of the T1RT, and IR of the L/M ratio (Fig. 2). Bland–Altman analysis yielded narrow limits of agreement for pre-enhancement T1RT, RR of the T1RT, and IR of the L/M ratio.

T1 Relaxation Time Measurement

The average length of time between the date of Gd-EOB-DTPA-enhanced MRI and that of liver biopsy was 68 days (range 0–156 days). The mean ± SD of pre-enhancement T1RT was 822 ± 93 msec (range; 685–1037 msec). The mean ± SD of RR of T1RT was 53.8 ± 10.2% (range; 34.5–68.7%). The distribution (box-and-whisker plots) of the pre-enhancement T1RT and the RR of the T1RT are shown in Figs. 3 and 4. The mean ± SD of pre-enhancement T1RT increased with the degree of fibrosis (F0-F1, 825 ± 90.1 msec, versus F2-F3-F4, 850 ± 94.1 msec, $P = 0.075$, F0-F1-F2, 819 ± 83.8 msec versus F3-F4, 875 ± 98.6 msec, $P = 0.41$ and F0-F1, 825 ± 90.1 msec versus F2-F3, 829 ± 92.7 msec, $P = 0.96$.

The mean ± SD of RR determined using T1RT decreased with the degree of fibrosis (F0-F1, 58.5 ± 6.2%, versus F2-F3-F4, 48.8 ± 11.7%, $P = 0.010$, F0-F1-F2, 58.2 ± 6.2% versus F3-F4, 45.5 ± 12.3%, $P = 0.010$ and F0-F1, 58.5 ± 6.2% versus F2-F3, 52.1 ± 12.0%, $P = 0.0038$).

Thus, the RR of T1RT showed significant differences to differentiate F0-F1 from F2-F3-F4, F0-F1-F2 from F3-F4, F0-F1 from F2-F3, although the pre-enhancement T1RT did not show significant differences.

Signal-Based Liver-to-Muscle Ratio

The mean ± SD of IR of L/M ratio was 59.7 ± 19.4% (range; 24.2–83.2%). The mean ± SD of IR of L/M ratio decreased with the degree of fibrosis (F0-F1, 61.5 ± 19.6%, versus F2-F3-F4, 55.2 ± 11.8%, $P = 0.47$, F0-F1-F2, 59.8 ± 17.2% versus F3-F4, 54.9 ± 13.3%, $P = 0.21$ and F0-F1, 61.5 ± 19.6% versus F2-F3, 55.5 ± 7.3%, $P = 0.52$). Thus, the IR of L/M ratio did not show significant differences to differentiate F0-F1 from F2-F3-F4, F0-F1-F2 from F3-F4, F0-F1 from F2-F3.

The distribution (box-and-whisker plots) of the IR of L/M ratio is shown in Fig. 5.

LSM of US Elastography

The average length of time between the dates of the FibroScan and the liver biopsy was 53 days (range 0–143 days). The mean ± SD of LSM obtained using the FibroScan was 12.4 ± 15.8 kPa (range; 2.7–55.0 kPa). The mean ± SD of IQR on the FibroScan was 2.3 ± 3.3 kPa (range; 0–11.9 kPa) for all patients. The distribution (box-and-whisker plots) of the LSM is shown in Fig. 6.

The LSM increased in line with the degree of fibrosis (F0-F1, 5.4 ± 2.2 kPa versus F2-F3-F3, 19.3 ± 15.5 kPa, $P = 0.0011$, F0-F1-F2, 6.8 ± 3.6 kPa versus F3-F4, 23.8 ± 17.1 kPa, $P = 0.0029$, and F0-F1, 5.4 ± 2.2 kPa versus F2-F3, 11.4 ± 7.2 kPa, $P = 0.0098$).

Thus, the LSM of FibroScan showed significant differences to differentiate F0-F1 from F2-F3-F4, F0-F1-F2 from F3-F4, F0-F1 from F2-F3.

Correlation Between T1 Mapping, Signal-Based Liver-to-Muscle Ratio, and FibroScan

The average length of time between the date of Gd-EOB-DTPA-enhanced MRI and FibroScan was 16 days (range, 0–27 days). Figure 7 shows a correlation diagram regarding the Gd-EOB-DTPA-enhanced MRI and FibroScan. In comparing the levels of LSM obtained using FibroScan with the RR of T1RT, a negative correlation was found ($r = -0.65$, $P = 0.00005$).

In discriminating between patients with F3-F4 liver fibrosis, the AUCs from the ROC analysis were 0.83 (cutoff value 53.5%. sensitivity 0.80, specificity 0.71) for the RR of T1RT and 0.83 for the LSM (cutoff value 13.8 kPa, sensitivity 0.73, specificity 0.90) (Fig. 8a, Table 1). The AUCs from the ROC analysis in patients with F2-F3-F4 fibrosis on histology were 0.72 (cutoff value 56.8%, sensitivity 0.71, specificity 0.64) for the RR of T1RT and 0.88 (cutoff value 9.6 kPa, sensitivity 0.76, specificity 0.92) for the LSM (Fig. 8b, Table 1). In discriminating between patients with F2-F3 liver

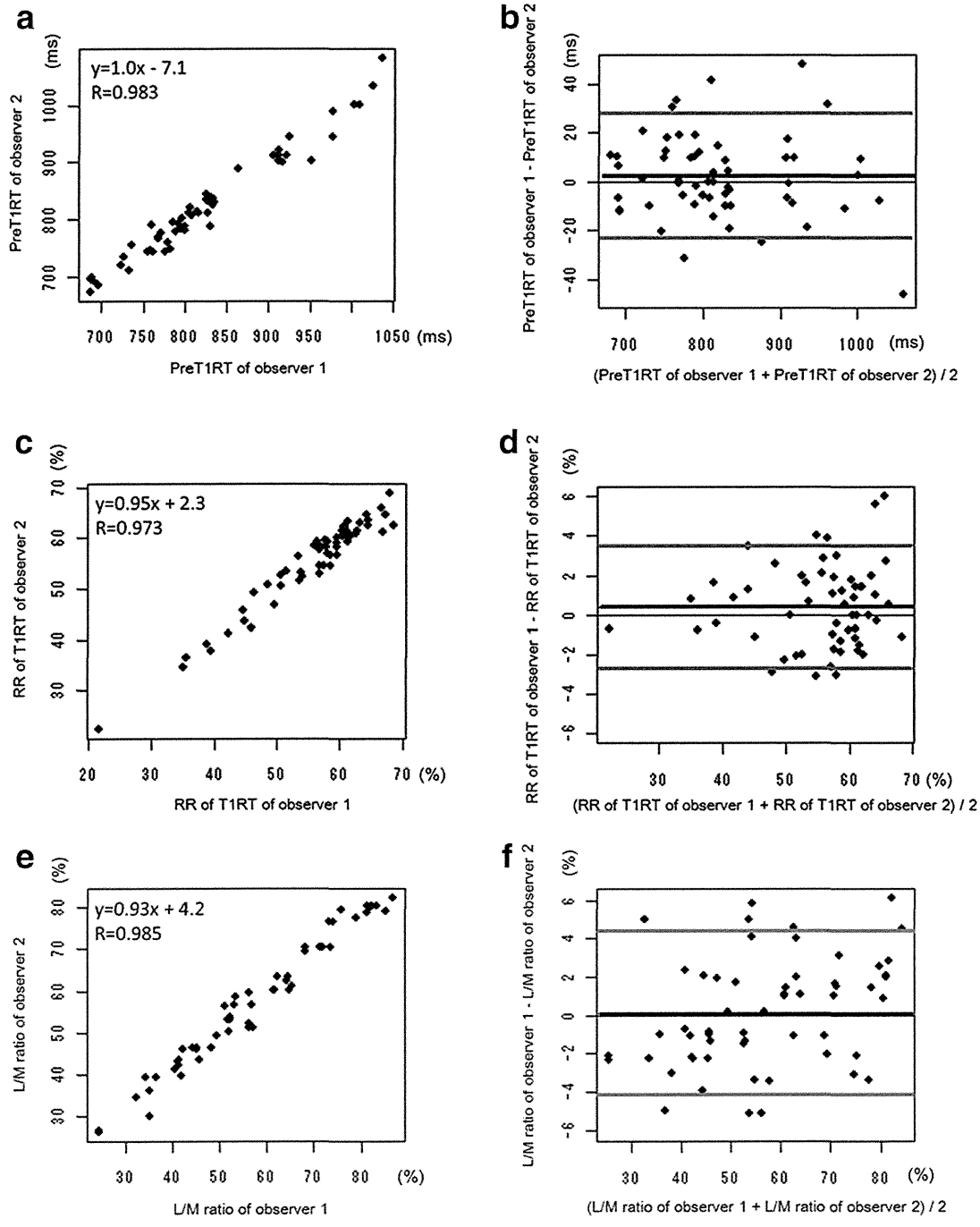

Figure 2. Agreement between the two observers' measurements. Simple regression analyses (a: pre-enhancement T1RT, c: RR of the T1RT, e: IR of the L/M ratio) and Bland–Altman analyses of agreement (b: pre-enhancement T1RT, d: RR of the T1RT, f: IR of the L/M ratio) between the two measurements are displayed. Simple regression analysis showed a high correlation between the means of the observers' manual measurements of pre-enhancement T1RT, RR of the T1RT, IR of the L/M ratio in the liver parenchyma. Bland–Altman analysis yielded narrow limits of agreement of −23 to 28 msec for pre-enhancement T1RT, of −2.7 to 3.5% for RR of the T1RT, and of −4.1 to 4.4% for the L/M ratio. Black line (center) = mean of differences. Gray lines (top and bottom) = upper and lower limits of agreement (mean difference, ±2 SD). pre T1RT; precontrast T1 relaxation time, RR of T1RT; reduction rate of T1 relaxation time, L/M ratio; liver to paraspinal muscle ratio.

fibrosis, the AUCs from the ROC analysis were 0.68 (cutoff value 59.4%. sensitivity 0.64, specificity 0.72) for the RR of T1RT and 0.81 for the LSM (cutoff value 5.5 kPa, sensitivity 0.81, specificity 0.71) (Fig. 8c, Table 1).

The capability of LSM was better than that of RR of T1RT, pre-enhancement T1RT, and L/M ratio to differentiate $F \geq 2$, but LSM and RR of T1RT showed the same value to differentiate $F \geq 3$ (Fig. 8a–c, Table 1).

DISCUSSION

We assessed the efficacy of T1RT on Gd-EOB-DTPA-enhanced MRI (T1 mapping) for the evaluation of the

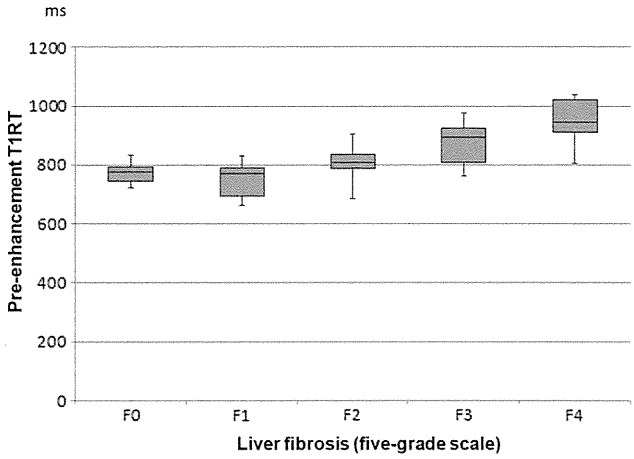

Figure 3. Box-and-whisker plots of pre-enhancement T1 relaxation time. The distribution of pre-enhancement T1RT is shown for New Inuyama Classification fibrosis stages (F0–F4) in patients who had liver biopsy. F0 = no fibrosis; F1 = fibrous portal expansion; F2 = bridging fibrosis (portal-portal or portal-central linkage); F3 = bridging fibrosis with lobular distortion (disorganization); and F4 = cirrhosis.

severity of liver fibrosis, in patients with chronic liver diseases. In our study, we found that the RR of T1RT measured before and 18 minutes after Gd-EOB-DTPA injection was inversely correlated with the LSM index determined by FibroScan. Both the RR of T1RT and the LSM measurement using FibroScan performed well (AUC: RR = 0.83 and LSM = 0.83) in the diagnosis of patients with fibrosis of grade $F \geq 3$. However, the use of RR of T1RT (AUC: 0.72) for the diagnosis of patients with fibrosis of grade $F \geq 2$ seemed to be somewhat less sensitive than the LSM (AUC: 0.88),

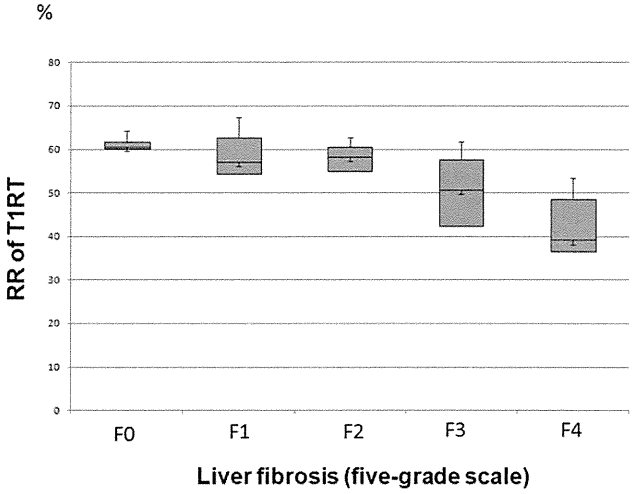

Figure 4. Box-and-whisker plots of reduction rate of T1 relaxation time on Gd-EOB-DTPA-enhanced MRI. The distribution of RR of T1RT on Gd-EOB-DTPA-enhanced MRI is shown for fibrosis stages (F0–F4) in patients who had liver biopsy. RR of T1RT of the liver parenchyma is defined as follows; RR = [(T1pre – T1post) / T1pre] × 100 (%), where T1pre is T1RT at pre-enhancement and T1post is T1RT at post-enhancement (18 min). F0 = no fibrosis; F1 = fibrous portal expansion; F2 = bridging fibrosis (portal-portal or portal-central linkage); F3 = bridging fibrosis with lobular distortion (disorganization); and F4 = cirrhosis.

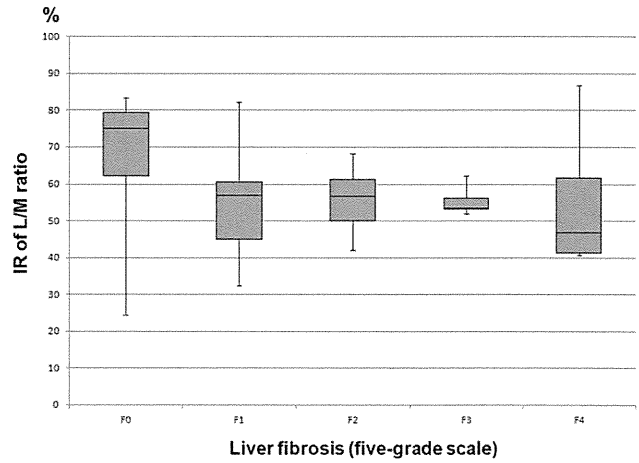

Figure 5. Box-and-whisker plots of increasing rate of liver to paraspinal muscle ratio on Gd-EOB-DTPA-enhanced MRI. The distribution of increasing rate (IR) of signal-based liver to paraspinal muscle ratio (L/M ratio) on Gd-EOB-DTPA-enhanced MRI is shown for fibrosis stages (F0–F4) in patients who had liver biopsy. IR of L/M ratio of the liver parenchyma is defined as follows; IR of the L/M ratio = [(L/M ratio post- – L/M ratio pre) / L/M ratio pre] × 100%, where L/M ratio pre is L/M ratio at pre-enhancement and L/M ratio post is L/M ratio at post-enhancement (20 min). F0 = no fibrosis; F1 = fibrous portal expansion; F2 = bridging fibrosis (portal-portal or portal-central linkage); F3 = bridging fibrosis with lobular distortion (disorganization); and F4 = cirrhosis.

because a certain degree of overlap among lower stages of liver fibrosis existed. Therefore, the RR of T1RT and the LSM of FibroScan were not equivalent, especially in patients with mild fibrosis. But T1RT by noninvasive means may be available for the diagnosis of relatively severe liver cirrhosis (fibrosis of grade $F \geq 3$), and be used as an alternative to FibroScan. In our study, the RR of T1RT and LSM of FibroScan showed significant differences to differentiate $F \geq 2$

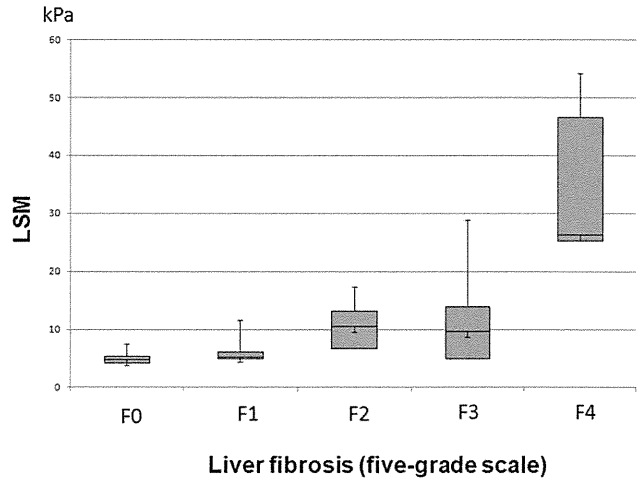

Figure 6. Box-and-whisker plots of liver stiffness measurement on FibroScan. The distribution of LSM of FibroScan in patients who had liver biopsy. Box-and-whisker plots of LSM on FibroScan is shown for fibrosis stages (F0–F4) in patients who had liver biopsy. F0 = no fibrosis; F1 = fibrous portal expansion; F2 = bridging fibrosis (portal-portal or portal-central linkage); F3 = bridging fibrosis with lobular distortion (disorganization); and F4 = cirrhosis.

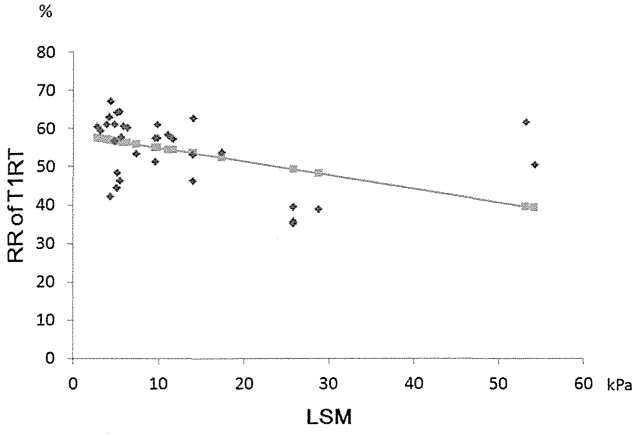

Figure 7. Correlation diagram between LSM of FibroScan and reduction rate of T1RT on Gd-EOB-DTPA-enhanced MRI. Spearman rank correlation was used to investigate the relation between LSM and RR of T1RT. There is a negative correlation between LSM and RR ($r = -0.65$, $P = 0.00005$).

and $F \geq 3$, although the pre-enhancement T1RT and IR of L/M ratio did not show significant differences. Thus, the RR of T1RT is helpful for staging of liver cirrhosis, especially in patients with $F \geq 3$.

Liver fibrosis occurs due to a scarring process and deposition of collagen and causes hepatic dysfunction. However, the relationship between hepatocyte function and fibrosis is not well understood. To facilitate a more quantitative evaluation of liver cirrhosis on Gd-EOB-DTPA-enhanced MRI, we focused on T1RT. This was due to the fact that changes in the T1 relaxation rate were considered directly proportional to the amount of contrast agent taken up by hepatocyte cells (23). On the other hand, changes in the signals of T1-weighted images after the injection of Gd-related contrast agent, such as Gd-EOB-DTPA, were not considered directly proportional to the concentration of contrast agent (24) because MR signal intensity does not show a linear relationship with the Gd-EOB-DTPA concentration. In recent reports, liver function studies using signal enhancement with Gd-EOB-DTPA (25,26) have been analyzed using ROI-based measurements; for example, the signal from the liver was subtracted between the phases or normalized with that in other organs. However, in these measurements there was a risk that signal enhancement could lose objectivity because the pixel value could be easily affected by extrinsic factors such as receiver gain and tuning MRI radiofrequency coils. Therefore, we believed that T1RT is a better method to evaluate the uptake of Gd-EOB-DTPA to the liver.

When liver MRI is performed for the purpose of detection and characterization of liver tumors, we suggest that T1 mapping could be used as an adjunct to routine imaging, to assess the degree of liver fibrosis in patients with liver diseases. Liver fibrosis can occur either homogeneously or heterogeneously. Therefore, we suggest that the grading of fibrosis should be estimated using T1 mapping in each liver segment, using a classification system such as that developed by Couinaud. Our method using T1RT measurement provides an evaluation of parenchymal changes in different liver segments, enabling accurate evaluation of disease severity in cases in which the fibrosis is not uniform across the entire liver.

Gd-EOB-DTPA-enhanced MRI allows the assessment of not only liver cirrhosis, but also hepatic tumors. In particular, this modality has the potential for early detection of HCC (12,13). FibroScan has a disadvantage of no combination with grayscale sonography for screening of liver tumors, because FibroScan is a dedicated device for the evaluation for liver stiffness. The development of a noninvasive method for the assessment of liver fibrosis involving T1RT represents a major advance in the management of chronic liver diseases. As several authors have stated, evaluation of the kinetic distribution of Gd-EOB-DTPA during the hepatobiliary phase is a promising method for understanding hepatocyte function (14–16,27). The difference in contrast between liver tumors and the parenchyma is affected by liver function, which is mediated by hepatocyte cells.

Noninvasive imaging of liver fibrosis, involving modalities such as US, computed tomography (CT), and MRI, is currently used in patients with chronic liver disease and suspected HCC. In particular, US elastography (7,8) and MR elastography (28,29) are receiving increasing attention. US elastography has been recognized as the easiest device for noninvasive imaging. FibroScan is considered a reliable method for the diagnosis of severe fibrosis and cirrhosis (30), but a certain degree of overlap among lower stages of liver fibrosis has been reported (31). Limitations associated with the FibroScan should be mentioned and include its use regarding obese patients, patients with a narrow intercostal space, and patients with ascites, liver atrophy, space occupying lesions in the liver (32), and the exclusion of the left lobe due to heartbeat and depth location of imaging. In addition, one-dimensional (1D) US imaging with the propagation speed of a wave, using pulse-echo US for FibroScan, is different from two-dimensional (2D) MRI such as T1 mapping with Gd-EOB-DTPA. Another promising method is MR elastography. This modality quantifies the viscoelastic parameters of the liver by measuring acoustic shear waves through the liver tissue (28). Several reports support the observation that a normal mean liver stiffness value obtained using MR elastography in the setting of chronic liver disease is consistent with a liver fibrosis score of F0 on pathology (28), while other fibrosis scores (F1–F4) are also diagnosed accurately (28,33). This method does not require MR contrast agents and may be more cost-effective than T1RT with Gd-EOB-DTPA, although additional equipment is required for MR elastography.

Diffusion-weighted imaging (DWI) of the liver is also useful for assessing liver fibrosis. Decreased apparent diffusion coefficient (ADC) is caused by the decrease in total hepatic blood flow in cirrhosis. Intravoxel incoherent motion (IVIM) analysis is based on a method that enables separate determination of coefficients with molecular diffusion of water and microcirculation of blood in the capillary network in each imaging voxel. IVIM may serve as a valuable tool for assessing liver fibrosis, because it reflects decreased capillary

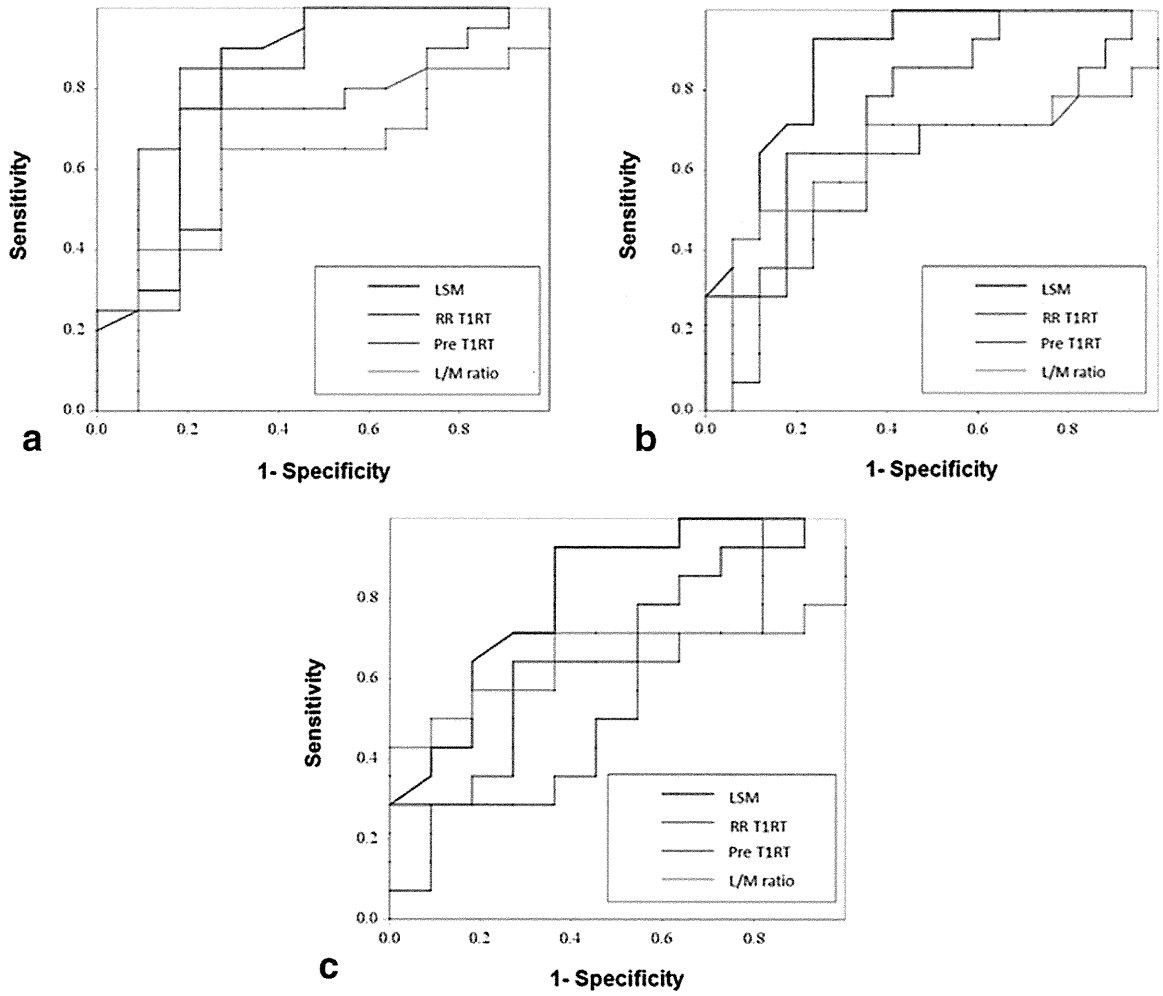

Figure 8. ROC curves of RR of T1RT, LSM, pre T1RT, and liver to paraspinal muscle ratio (L/M ratio) for F3-F4 fibrosis stages. On the ROC curves of RR of T1RT, LSM, pre-enhancement T1RT, and liver to paraspinal muscle ratio (L/M ratio), area under the receiving operating curve (AUC), cutoff value between F3-F4 and F0-F1-F2, sensitivity and specificity are shown in the Table 1. **a:** ROC curves of LSM (AUC, 0.83) and RR of T1RT (AUC, 0.83) were superior to pre-enhancement T1RT (AUC, 0.67) and L/M ratio (AUC, 0.61). **b:** ROC curves of RR of T1RT, LSM, pre-enhancement T1RT and L/M ratio for F2-F3-F4 fibrosis stages. On ROC curves of RR of T1RT, LSM, pre-enhancement T1RT, and L/M ratio, LSM (AUC, 088) was superior to RR of T1RT (AUC, 0.72), pre-enhancement T1RT (AUC, 0.59) and L/M ratio (AUC, 0.63). Cutoff value, sensitivity, and specificity are shown in Table 1. **c:** ROC curves of RR of T1RT, LSM, pre-enhancement T1RT and L/M ratio for F2-F3 fibrosis stages. On ROC curves of RR of T1RT, LSM, pre-enhancement T1RT, and L/M ratio, LSM (AUC, 081) was superior to RR of T1RT (AUC, 0.68), pre-enhancement T1RT (AUC, 0.50), and L/M ratio (AUC, 0.65). Cutoff value, sensitivity, and specificity are shown in Table 1.

perfusion as well as alterations in pure molecular water diffusion in cirrhotic livers (34). But technical factors, such as cardiac motion limiting evaluation of the left hepatic lobe and respiratory motion effecting ADC values in the right hepatic lobe, need to be addressed with respiratory-triggered techniques.

Perfusion-weighted imaging (PWI) of the liver is employed by dual-input one-compartment analysis and has permitted measurement of flow parameters such as hepatic arterial/portal venous inflow rate, absolute hepatic arterial/portal venous blood flow, hepatic arterial/portal venous fraction, mean transit time, and distribution volume. PWI is correlated with the severity of cirrhosis and portal hypertension (35). But PWI cannot directly reflect the fibrosis component alone, because the analysis is substantially based on vascular flow and perfusion.

The present study had some limitations. First, T1 mapping may not provide the T1RT at exactly the same location in the liver as the FibroScan and liver biopsy, due to the fact that the T1 mapping image in our study was obtained as a single axial slice. Second, our analysis using T1 mapping could not always reflect the fibrosis component alone. There was a lack of analysis of other factors that might influence elasticity, such as steatosis, iron overload, vascular flow, and perfusion (36). In addition, the relationship between fibrosis (F-factor) and necroinflammation (activity) on histological examination was not investigated in our study. Further analysis is required. Third, the uptake of Gd-EOB-DTPA in the hepatocyte allows shortening T1RT, which links to the Gd-EOB-DTPA concentration at the hepatobiliary phase. The contrast agent enters the hepatocytes through the

Table 1
Receiver Operating Characteristic (ROC) Analysis

	LSM	RR of T1RT	Pre T1RT	L/M ratio
F012–34				
AUC	0.83	0.83	0.67	0.61
Cutoff	13.8	53.5	863	56.7
Sens.	0.73	0.80	0.72	0.65
Spec.	0.90	0.71	0.75	0.73
F01–234				
AUC	0.88	0.72	0.59	0.63
Cutoff	9.60	56.8	831	56.7
Sens.	0.76	0.71	0.64	0.71
Spec.	0.92	0.64	0.64	0.64
F01–23				
AUC	0.81	0.68	0.50	0.65
Cutoff	5.50	59.4	831	56.7
Sens.	0.81	0.64	0.54	0.71
Spec.	0.71	0.72	0.64	0.63

LSM, liver stiffness measurement (unit, kPa); RR of T1RT, reduction rate of T1 relaxation time (unit, %); pre T1RT; precontrast T1 relaxation time (unit, msec); L/M ratio, liver to paraspinal muscle ratio on signal based measurement (unit, %); F012–34, fibrosis grade of New Inuyama Classification; F012 versus F34, F01–234, F01 versus F234, F01–23; F01 versus F23; AUC, area under the ROC curve; Sens., sensitivity; Spec., specificity.

organic anion transporting polypeptides (OATP) 1B1 (OATP1B1) and/or OATP1B3, and it is excreted into the bile via multidrug resistance protein 2 (MRP2) (37). But the parameter of T1RT cannot distinguish the excretion from the uptake of Gd-EOB-DTPA, because the concentration of these transporters in patients with liver fibrosis is unknown. Therefore, we should know the expression rate of OATP1B1, OATP1B3, and MRP2 in grading of liver cirrhosis. Further elucidation to assess the correlation between the expression of sinusoidal and canalicular transporters and T1RT of Gd-EOB-DTPA-enhanced MRI is needed.

Fourth, biopsy specimens that do not meet the scoring criteria of the New Inuyama Classification are associated with a high risk of understaging (38). In addition, further investigation is required as to whether or not there are differences between specimen biopsies and images (T1 mapping and FibroScan). Fifth, the effects of cardiac function were not investigated at FibroScan examination, although patients had no past history of cardiac diseases (cardiac function may be a potentially influential factor in the use of FibroScan) (39). Sixth, the maximum length of time between the date of Gd-EOB-DTPA-enhanced MRI (or FibroScan) and that of liver biopsy was 156 (or 143) days. In these patients, the amount of fibrosis may change. However, we believe there may be no apparent change of liver fibrosis in these patients, because the progression rate of liver fibrosis is known as 0.1 unit/year (for example, it takes ~10 years from F1 to F2) (40).

In conclusion, the estimation of the RR determined using T1RT of T1 mapping with Gd-EOB-DTPA is a noninvasive tool for assessing liver fibrosis, and it is inversely correlated with the LSM obtained using FibroScan. Our result proved the noninferiority of T1 mapping for noninvasive diagnosis of liver fibrosis in comparison with US elastography, especially in patients with severe fibrosis, such as F3-F4, because the diagnostic accuracy of T1 mapping is almost the same as that of US elastography. But these interpretations remain speculative due to the limited number of patients enrolled in our study. Further studies are recommended to confirm the superiority of T1 mapping in the assessment of liver fibrosis because this new technique has not yet been validated in large clinical trials.

REFERENCES

1. Schiff ER, Lee SS, Chao YC, et al. Long-term treatment with entecavir induces reversal of advanced fibrosis or cirrhosis in patients with chronic hepatitis B. Clin Gastroenterol Hepatol 2011;9:274–276.
2. Chang TT, Liaw YF, Wu SS, et al. Long-term entecavir therapy results in the reversal of fibrosis/cirrhosis and continued histological improvement in patients with chronic hepatitis B. Hepatology 2010;52:886–893.
3. Poynard T, Bedossa P, Opolon P. Natural history of liver fibrosis progression in patients with chronic hepatitis C. The OBSVIRC, METAVIR, CLINIVIR, and DOSVIRC groups. Lancet 1997;349: 825–832.
4. Parkes J, Guha IN, Roderick P, Rosenberg W. Performance of serum marker panels for liver fibrosis in chronic hepatitis C. J Hepatol 2006;44:462–474.
5. Bravo AA, Sheth SG, Chopra S. Liver biopsy. N Engl J Med 2001; 344:495–500.
6. Piccinino F, Sagnelli E, Pasquale G, Giusti G. Complications following percutaneous liver biopsy. A multicentre retrospective study on 68,276 biopsies. J Hepatol 1986;2:165–173.
7. Koizumi Y, Hirooka M, Kisaka Y, et al. Liver fibrosis in patients with chronic hepatitis C: noninvasive diagnosis by means of real-time tissue elastography—establishment of the method for measurement. Radiology 2011;258:610–617.
8. Tatsumi C, Kudo M, Ueshima K, et al. Noninvasive evaluation of hepatic fibrosis using serum fibrotic markers, transient elastography (FibroScan) and real-time tissue elastography. Intervirology 2008;51(Suppl 1):27–33.
9. Ziol M, Handra-Luca A, Kettaneh A, et al. Noninvasive assessment of liver fibrosis by measurement of stiffness in patients with chronic hepatitis C. Hepatology 2005;41:48–54.
10. Ichikawa T, Saito K, Yoshioka N, et al. Detection and characterization of focal liver lesions: a Japanese phase III, multicenter comparison between gadoxetic acid disodium-enhanced magnetic resonance imaging and contrast-enhanced computed tomography predominantly in patients with hepatocellular carcinoma and chronic liver disease. Invest Radiol 2010;45:133–141.
11. Zech CJ, Herrmann KA, Reiser MF, Schoenberg SO. MR imaging in patients with suspected liver metastases: value of liver-specific contrast agent Gd-EOB-DTPA. Magn Reson Med Sci 2007;6:43–52.
12. Kogita S, Imai Y, Okada M, et al. Gd-EOB-DTPA-enhanced magnetic resonance images of hepatocellular carcinoma: correlation with histological grading and portal blood flow. Eur Radiol 2010; 20:2405–2413.
13. Okada M, Imai Y, Kim T, et al. Comparison of enhancement patterns of histologically confirmed hepatocellular carcinoma between gadoxetate- and ferucarbotran-enhanced magnetic resonance imaging. J Magn Reson Imaging 2010;32:903–913.
14. Tsuda N, Okada M, Murakami T. Potential of gadolinium-ethoxybenzyl-diethylenetriamine pentaacetic acid (Gd-EOB-DTPA) for differential diagnosis of nonalcoholic steatohepatitis and fatty liver in rats using magnetic resonance imaging. Invest Radiol 2007;42:242–247.
15. Tsuda N, Okada M, Murakami T. New proposal for the staging of nonalcoholic steatohepatitis: evaluation of liver fibrosis on Gd-EOB-DTPA-enhanced MRI. Eur J Radiol 2010;73:137–142.
16. Katsube T, Okada M, Kumano S, et al. Estimation of liver function using T1 mapping on Gd-EOB-DTPA-enhanced magnetic resonance imaging. Invest Radiol 2011;46:277–283.